Title
High Resolution Magnetic Resonance Imaging via Artificial Intelligence and Radiofrequency Coil Design

Author
Lin, Jiahao

Publication Date
2023

Peer reviewed|Thesis/dissertation

UNIVERSITY OF CALIFORNIA

Los Angeles

High Resolution Magnetic Resonance Imaging via Artificial Intelligence and Radiofrequency Coil Design

A dissertation submitted in partial satisfaction of the requirements for the degree Doctor of Philosophy in Electrical and Computer Engineering

by

Jiahao Lin

ABSTRACT OF THE DISSERTATION

High Resolution Magnetic Resonance Imaging

via Artificial Intelligence and Radiofrequency Coil Design

by

Jiahao Lin

Doctor of Philosophy in Electrical and Computer Engineering

University of California, Los Angeles, 2023

Professor Robert N. Candler, Chair

Magnetic resonance imaging (MRI) is a non-invasive imaging technique that can produce high spatial resolution 3D images, especially for non-bony parts or soft tissues. Higher imaging resolution is usually preferred, to detect small lesions or irregularities in the imaging subject. This dissertation presents two projects that aims for high-resolution MRI. In the first project, we designed a single-loop miniature flexible coil that can be surgically positioned millimeters from the pituitary gland, enabling high-SNR pituitary MRI. We investigated the spatial distributions of the image SNR of the miniature coil, via both numerical simulation and phantom experiments. We also explored the feasibility of increased SNR within the pituitary gland based on simulated surgical placements. Compared to the commercial head coil, our miniature coil achieved up to a 19-fold SNR improvement within the region of interest, and the simulation and phantom

experiment reached a good agreement, with an error of 1.1% ± 0.8%. High resolution MRI scans further demonstrated the visual improvement of the miniature coil against the commercial head coil. The cross-validation of the simulation and the phantom experiment showed the potential of using the numerical simulation model to accelerate the coil design prototyping and iteration and to optimize coil design in the future. The clinical application study describes a transnasally-placed 2-cm flexible coil to improve the resolution of pituitary imaging. The coil is compatible with 95% of patients, can be successfully placed in contact with the sella in cadaver studies, shows no temperature changes in phantom studies during scanning, and improves the SNR of the pituitary by an order of 17. This study provides feasibility data for the promise of application to the clinical setting to improve the detection of small ACTH-secreting pituitary tumors when clinical pituitary MRI fails.

In the second project, we propose a novel slice-profile transformation super-resolution (SPTSR) framework with deep generative learning for through-plane super-resolution (SR) of multi-slice 2D TSE imaging. The deep generative networks were trained by synthesized low-resolution training input via slice-profile downsampling (SP-DS), and the trained networks inferred on the slice profile convolved (SP-conv) testing input for 5.5x through-plane SR. The network output was further slice-profile deconvolved (SP-deconv) to achieve an isotropic super-resolution. Compared to the state-of-the-art SMORE SR method, where the networks trained by conventional downsampling, our SPTSR framework demonstrated the best overall image quality from 50 testing cases, evaluated by two abdominal radiologists. The quantitative analysis cross-validated the expert reader study results. 3D simulation experiments confirmed the quantitative improvement of the proposed SPTSR and the effectiveness of the SP-deconv step, compared to 3D ground-truths. Ablation studies were conducted on the individual contributions of SP-DS and

SP-conv, networks structure, training dataset size, and different slice profiles.

The dissertation of Jiahao Lin is approved.

Achuta Kadambi

Aydin Babakhani

Kyunghyun Sung, Committee co-Chair

Robert N. Candler, Committee Chair

University of California, Los Angeles 2023

Table of Contents

List of Figures

and the normalized $B_{1xy\ effective}$. The simulation fields were normalized based on the maximum $B_{1xy\ effective}$ field at d = 4.5 mm.

Figure 3.6: High-resolution PD-TSE image comparisons, using the commercial head coil (left), and the pituitary miniature flexible coil at θ = 0° (middle) and θ = 60° (right). The voxel size is 0.2 × 0.2 × 0.7 mm^3. Imaging planes were selected 1 cm from the coil. Images from miniature flexible coil are at the same window level, while the image from the commercial head coil is at its own window level for better visualization.

Figure 3.7: Mean SNR from the scan at various ROI depths and rotation angles, compared with the corresponding mean of the normalized effective transverse B_1 field from the simulation. The simulated fields were normalized to a single point, the mean $B_{1xy\ effective}$ at θ = 0° at 4.5 mm below the coil.

Figure 3.8: Bland-Altman plot for SNR of two repeated SD PD-TSE scans, SNR_1 and SNR_2. X-axis is the mean of the two scans, and Y-axis is the percentage difference.

Figure 4.1: Coil surgical placement example on the retrospective patient image. SNR improvement using the miniature coil compared to a commercial head coil was estimated using the simulated effective field at θ = 30°. The red ellipse indicates the location of the pituitary gland.

Figure 4.2: Anatomic measurements of the sphenoid sinus in 50 patients using magnetic resonance imaging T1 with contrast images in the midline sagittal (a) and axial (b) planes. The distributions of the craniocaudal sphenoid distance at various degrees and the lateral intercarotid distance (c).

Figure 4.3: Electromagnetic simulations with a 2 cm radiofrequency coil predicting signal-to-noise ratio increases at various distances from the coil and with various coil rotation angles relative to the horizontal MRI head holder and superposition of these simulations on an MRI T1 with contrast sphenoid sinus region.

Figure 4.4: (a) The coil was designed with flexibility for transnasal application and (b) a protective coating was applied to the coil to maintain this flexibility.

Figure 4.5: (a) Cadaveric preparation of the sella with the removal of sphenoid septae and mucosa, (b) placement of collagen sponge in clival recess to eliminate air-bone interface artifact, (c) placement of exible mini coil at 0 degrees, (d) filling of the sphenoid sinus with collagen sponge.

Figure 4.6: Cadaver heads with the placement of the flexible coil on T1-MPRAGE images with 0.9 mm slice thickness (A), 0.4 mm slice thickness (B), and 0.2mm slice thickness (C). The images were compared with the images from the Siemens 20-channel Head/Neck coil at the same resolutions. The pituitary gland region of interest (marked by white dotted circle) was divided into 4 sub-regions with 3 mm width: Region a, Region b, Region c, and Region d (D). The noise region of interest is identified by the blue circle.

Figure 4.7: (a) A coronal view of the pituitary gland using high-resolution Proton density (0.2mm x 0.2mm x 0.7mm) image with the flexible coil in a cadaveric specimen, (b) the annotated image showing highlighted pituitary gland (yellow outline) and hypointensity (red outline). (c, d) Corresponding coronal sections with reticulin stain and H&E stain show a cyst like structure in the lateral aspect of this gland.

Figure 4.8: (a) Meat phantom with direct coil placement and thermometer placement and (b) schematic illustrations of the two temperature measuring sites. (c) Temperature recordings at measuring sites S1 and S2 for the 15-minute fast low angle shot three-dimensional imaging (FL3D) sequence scan.

Figure 8.1: The overall SPTSR framework, with training flow (top) and inference flow (bottom).

Figure 8.2: a) The proposed SP-downsampling method. Each line of pixels is acquired by multiplying the slice profile PSF_{SI} of length L, to the same physical location on the cropped coronal scan; b) The KS-ZF downsampling method. Each slice of image is transformed to the frequency domain via FFT, cropped its center lines and iFFT back to the downsampled image.

Figure 8.3: The down-sampling method visual comparison. a) the conventional KS-ZF downsampled image patch, b) the SP-downsampled image patch, c) the reformatted axial patch, and d) the SP-convolved axial patch. Thickness in each patch represents the voxel thickness in the AP-direction. All patches are bilinear interpolated to demonstrate the visual differences.

Figure 8.4: The WGAN-GP based deep generative networks architecture of our proposed SPTSR framework.

Figure 8.5: The proposed SR inference flow. T2w-TSE axial scan is cropped and SP-convolved in the AP-direction to prepare the input for the deep generative networks. The output of the networks is still convolved in the AP-direction and is then transformed to isotropic SR volume via SP-deconvolution. Red patches represent coronal views and blue patches represent axial views. Patch thickness represents the voxel thickness in the through-plane of the patch.

Figure 9.1: The through-plane SR testing results with reformatted T2w axial scan input. a) and b) represents two image slices from two different testing subjects. From left to right: The T2w coronal scan of the subject, as a visual reference; the testing reformatted T2w axial scan as the inference input; the bilinear interpolation of the input; SMORE [26]; the baseline inference output with KS-ZF trained networks; the proposed SPTSR inference output with SP-downsampling trained network, and SP-convoluted inference input. Red arrows indicate the structural differences between the baseline results and the proposed results.

Figure 9.2: Two radiologists qualitatively assessed the diagnostic quality of Bilinear Interpolation (BI), SMORE [8], KS-ZF trained networks (baseline), SPTSR (proposed), for sharpness, artifacts, noise and overall image quality on a 1 to 4 scale (higher the better). The ratings were averaged from two readers. Error bar represents the standard deviations. Mann-Whitney U tests assessed whether the average scores were significantly different ($p<0.01$) among the four groups.

List of Tables

ACKNOWLEDGEMENTS

I would like to thank my advisor Kyunghyun Sung. He is extremely supportive and provides precious mentorship, not only in academics and research but in all aspects of my life. He is always encouraging and provides direction, guiding me through all the ups and downs in my academic pathways.

I would like to thank all my collaborators and co-workers. Thanks to Dr. Robert N. Candler and Dr. Siyuan Liu, Dr. Marvin Bergsneider, Dr. Rock Hadley, Dr. Giyarpuram N. Prashant, Dr. Sophie Peeter, Dr. Kunal S Patel for our collaborations in developing the miniature flexible coil for the pituitary gland. It is truly an exceptional multidisciplinary collaboration. Thanks to Dr. Qi Miao and Dr. Chuthaporn Surawech for helping design the prostate reader study and meticulously grading 50 testing subjects. Thanks to Dr. Steven S. Raman, Dr. Kai Zhao, and Dr. Holden H. Wu for improving and refining our super-resolution research.

I would like to thank my committee chair and members, Dr. Rob Candler, Dr. Achuta Kadambi, and Dr. Aydin Babakhani, for providing comments and feedback to guide this dissertation to completion.

I would like to thank my fellow friends and colleagues in MRRL, including Fadil Ali, Xinzhou Li, Zhaohuan Zhang, Xinran Zhong, Tess Armstrong, Shu-fu Shih, Chang Gao, Haoxing Zheng, Qing Dai, etc. I would forever appreciate the camaraderie between us.

Last but not least, I would like to thank my parents and my wife for your unconditional love.

VITA

EDUCATION

UNIVERSITY OF CALIFORNIA, LOS ANGELES — **Los Angeles, CA**
Master of Science, Electrical and Computer Engineering — *9/2014-6/2016*

UNIVERSITY OF CALIFORNIA, LOS ANGELES — **Los Angeles, CA**
Bachelor of Science, Physics — *9/2010-6/2014*

PUBLICATIONS

J. Lin, Q. Miao, C. Surawech, S. S. Raman, K. Zhao, H. Wu, K. Sung, "High-Resolution 3D MRI With Deep Generative Networks via Novel Slice-Profile Transformation Super-Resolution," in *IEEE Access*, vol. 11, pp. 95022-95036, 2023.

S. Liu, KS Patel, S. Peeters M., **J. Lin**, A.C. DiRisio, H. Vinters, R. Candler, K. Sung, M. Bergsneider, "Flexible In-Cavity MRI Receiving Coil for Ultrahigh Resolution Imaging of the Pituitary Gland", Research Square; 2023. doi: 10.21203/rs.3.rs-2880527/v1.

S. Liu, **J. Lin**, M. Bergsneider, J. R. Hadley, N. G. Prashant, S. Peeters, R. Candler, K. Sung, "Experimental and Numerical Simulation of the Miniature Flexible Coil for High-SNR Pituitary MRI", International Society for Magnetic Resonance in Medicine, May 07-12, 2022.

J. Lin, Q. Miao, C. Surawech, S. S. Raman, H. Wu, K. Sung, "Super-resolution MRI using Novel Slice-profile Based Transformation for Multi-slice 2D TSE Imaging", International Society for Magnetic Resonance in Medicine, May 07-12, 2022.

J. Lin, S. Liu, M. Bergsneider, J. R. Hadley, N. G. Prashant, S. Peeters, R. Candler, K. Sung, "A Miniature Flexible Coil for High-SNR MRI of the Pituitary Gland". IEEE Access, 10, 12619–12628. 2022.

J. Lin, S. Liu, R, Hadley, M. Bergsneider, G. Prashant, S. Peeters, R. Candler, K. Sung, " Exploration of the Surgical Placement of the Local Pituitary Coil for Microadenomas", International Society for Magnetic Resonance in Medicine, May 15-20, 2021.

S. Peeters M., S. Liu, **J. Lin**, R. Candler, K. Sung, G. Prashant, M. Bergsneider, "Signal to Noise Ratio Increases with Miniature Surface Coil Position as Demonstrated by Both Numerical Simulation and Experimental Validation", J Neurol Surg B Skull Base 2021; 82(S 02): S65-S270

J. Lin, F. Ali, and K. Sung, "Volumetric real-time imaging with deep-learning reconstruction", International Society for Magnetic Resonance in Medicine, May 10-13, 2019.

J. Lin, S. Lefkimmiatis, and K. Sung, "Deep Network Training Based Sparsity Model for Reconstruction", International Society for Magnetic Resonance in Medicine, Apr. 22-27, 2017

Chapter 1: Introduction

Magnetic resonance imaging (MRI) is a non-invasive imaging technique that produces images of the internal characteristics of an object from its nuclear magnetic resonance (NMR) signals. MRI can produce high spatial resolution 3D images, especially for non-bony parts or soft tissues that contain water or fat. MRI scans are generally considered a safer imaging technique compared to X-ray and computed tomography (CT), as MRI does not emit the damaging ionizing radiation. Because of these advantages, MRI has become increasingly popular in radiology.

MRI follows a classic excitation-reception paradigm. The proton spins are aligned with the main magnetic field B_0 (Fig 1.1a). External excitations are applied to the proton spins in the form of Radiofrequency (RF) pulses. The proton spins are tilted and misaligned, and slowly recovers back to alignment with the B_0 field. RF receiver coils are placed close to the subject for the signal readout of this recovery (Fig 1.1b).

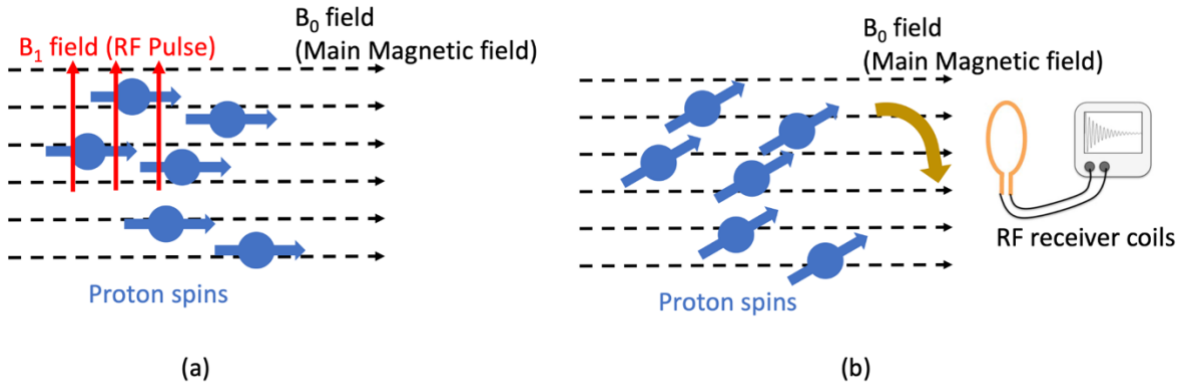

Figure 1.1: *(a) Proton spins align their orientations to B_0 field, and are disturbed by RF pulses, (b) spins recover to align with the B0 field. RF receiver coils are positioned close to the subject, for the signal readout of this recovery.*

Different tissues have different longitudinal relaxation time (T1), transverse relaxation time (T2), and proton density (PD). Pulse sequence diagrams are designed to capture the tissue contrast in the frequency domain. K-space raw data in the frequency domain is then reconstructed to MR images. To accelerate the scanning time, it is impractical to acquire fully sampled K-space data. Advanced reconstruction and post-processing are designed for incomplete K-space data.

Though the high-resolution MRI provides tremendous advantages in clinical diagnosis, especially in detecting smaller tumor lesions and diagnosing smaller body parts, it is non-trivial to increase the imaging resolution in practical ways under clinical protocols. Increase in resolution often comes with tremendous trade-offs, including longer scan times, worse imaging contrast and worse imaging artifacts, longer reconstruction times, more expensive MRI machines and higher maintenance costs.

Two projects are presented in this dissertation. In the first project, we designed a specific RF receiver coil for ultrahigh-resolution pituitary MRI; in the second project, we designed a super-resolution reconstruction framework for multi-slice 2D turbo-spin echo (TSE) pulse sequence.

In the first project, we designed a single-loop miniature flexible coil that can be surgically positioned millimeters from the pituitary gland, enabling high-SNR pituitary MRI. We investigated the spatial distributions of the image SNR of the miniature coil, via both numerical simulation and phantom experiments. We also explored the feasibility of increased SNR within the pituitary gland based on simulated surgical placements. Compared to the commercial head coil, our miniature coil achieved up to a 19-fold SNR improvement within the region of interest, and the simulation and phantom experiment reached a good agreement, with an error of 1.1% ± 0.8%. High resolution MRI scans further demonstrated the visual

improvement of the miniature coil against the commercial head coil. The cross-validation of the simulation and the phantom experiment showed the potential of using the numerical simulation model to accelerate the coil design prototyping and iteration and to optimize coil design in the future. The clinical application study describes a transnasally-placed 2-cm flexible coil to improve the resolution of pituitary imaging. The coil is compatible with 95% of patients, can be successfully placed in contact with the sella in cadaver studies, shows no temperature changes in phantom studies during scanning, and improves the SNR of the pituitary by an order of 17. This study provides feasibility data for the promise of application to the clinical setting to improve the detection of small ACTH-secreting pituitary tumors when clinical pituitary MRI fails.

In the second project, we propose a novel slice-profile transformation super-resolution (SPTSR) framework with deep generative learning for through-plane super-resolution (SR) of multi-slice 2D TSE imaging. The deep generative networks were trained by synthesized low-resolution training input via slice-profile downsampling (SP-DS), and the trained networks inferred on the slice profile convolved (SP-conv) testing input for 5.5x through-plane SR. The network output was further slice-profile deconvolved (SP-deconv) to achieve an isotropic super-resolution. Compared to the state-of-the-art SMORE SR method where the networks trained by conventional downsampling, our SPTSR framework demonstrated the best overall image quality from 50 testing cases, evaluated by two abdominal radiologists. The quantitative analysis cross-validated the expert reader study results. 3D simulation experiments confirmed the quantitative improvement of the proposed SPTSR and the effectiveness of the SP-deconv step, compared to 3D ground-truths. Ablation studies were conducted on the individual contributions of SP-DS and SP-conv, networks structure, training dataset size, and different slice profiles.

Miniature Flexible Coil for High-SNR MRI of the Pituitary Gland

Chapter 2: Introduction

There is a strong clinical need to improve the resolution of magnetic resonance imaging (MRI) for the detection of small pathological lesions. A salient example is Cushing's disease (CD): a potentially fatal disorder caused by an adrenocorticotropin hormone (ACTH)-producing pituitary tumor. While the median size of pituitary tumors (microadenomas) causing CD is 5 mm [1], a significant percentage is less than 3 mm in size [2]. Currently, 3T MRI is unable to detect up to 50% of microadenomas in CD [3]–[6]. This failure of diagnostic imaging thwarts the primary and optimal treatment of CD: surgical excision of the offending tumor. In such cases without an imaging-identifiable tumor, neurosurgeons must consider surgically "exploring" the anterior pituitary gland by making multiple parallel incisions typically spaced 2-3 mm apart with the hope of fortuitously encountering the tumor. In addition to the real possibility of not finding a tumor, this technique adds the risk of permanently damaging the normal gland.

Standard 3T pituitary MRI protocols generate multi-slice 2-dimensional (2D) images with a typical in-plane resolution of 0.7×0.7 mm^2 and a through-plane slice thickness of 3 mm [7]. When considering various shapes of the pituitary gland, partial volume averaging, and motion-related degradation [8], it is not surprising that MR images with an in-plane pixel size of 0.7 mm commonly fail to detect lesions smaller than 3 mm.

One of the common factors limiting MRI spatial resolution is signal-to-noise ratio (SNR). Two approaches for increased SNR are to use higher strengths (e.g., 7T MRI scanner [9], [10]) and to design application-specific radiofrequency (RF) coil arrays. These two are generally additive when combined with each other. Advancements have been made

with flexible RF coil arrays. Conforming the coil elements to the patient's surface anatomy achieves higher SNR in directly adjacent regions, which unfortunately, is of limited value for pituitary imaging given that the pituitary gland is located centrally within the cranium. Another approach to improve SNR is to place a separate receive-only RF coil in close proximity to the imaging target [11]. One example in clinical use, the endorectal coil designed for prostate imaging [12], has had limited use due to patient discomfort related to the relatively large diameter of the endorectal component. Chittiboina et al. [13] adopted the endorectal prostate coil for pituitary imaging. The study demonstrated a potential 10-fold increase in SNR by positioning the coil apparatus within the sphenoid sinus via a sublabial approach in a cadaver [13]. However, the design included a potential concern that the coil is needed to be positioned blindly, given the complete obstruction of the surgical corridor by the probe.

In this work, we report our initial evaluation of this novel coil design using a custom-built phantom which allowed us to precisely measure SNR. We designed a single-loop miniature flexible coil that could easily be placed via one nostril and optimally situated within the sphenoid sinus under direct endoscopic visualization (Fig. 1). Our coil design shares the same clinical implementation limitation as the previous study [13], in that it must be used as part of an elective surgical operation with the aim of removal of the tumor. The ideal orientation of the coil is parallel to the orientation of the main magnetic field, B_0. As the surgical positioning for endoscopic surgery is supine, our investigations of sphenoid sinus anatomy revealed that this coil orientation may not be anatomically possible in some cases. We therefore designed the phantom to allow us to study the effect of coil angulation relative to the B_0 field [14], [15]. The specific aims of our study are to 1) investigate spatial distributions of the image SNR for various coil rotation angles (θ) using

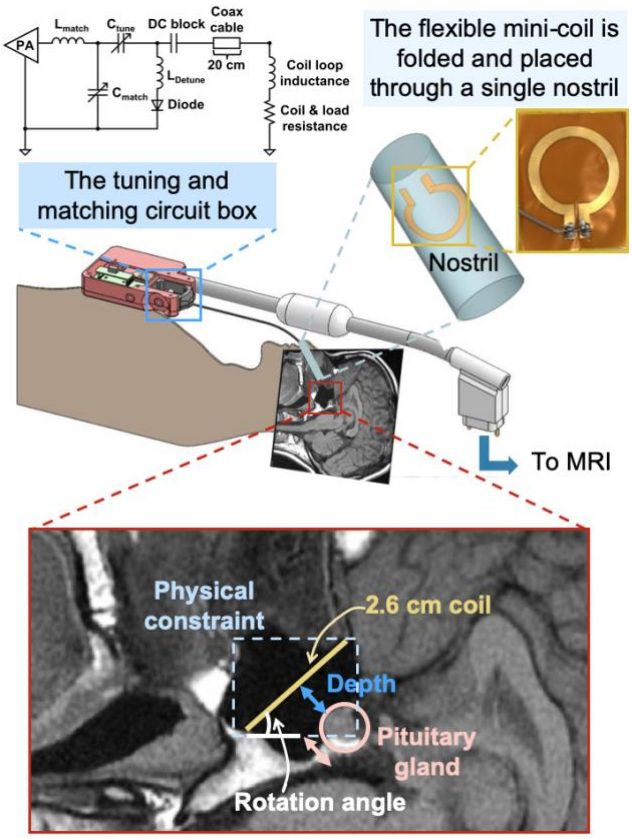

Figure 2.1: *Coil design and its surgical placement. The miniature coil is built on a flexible printed circuit board and connected to the tune and match box, which allows fine-tuning and matching of the coil remotely. The local pituitary coil is placed against the pituitary gland, and the coil rotation angle is defined as the angle between the coil plane and the scanner bed.*

a numerical simulation model and phantom experiments, and 2) test the feasibility of increased SNR within the pituitary gland based on simulated surgical placement results. The miniature coil was tested with high-resolution imaging to confirm its visual improvement against the commercial head coil. The coil design was iteratively developed by utilizing numerical electromagnetic simulations, and this cross-validation approach will be useful in further optimizing the coil in the future, including the potential to select an optimal coil from a predetermined range of coil shapes and sizes.

Chapter 3: Coil Design and Simulation

3.1 Design Optimization Related to Surgical Placement

From a coil design perspective, the coil diameter should not only be large enough to provide sufficient coverage for pituitary MRI but must also fit within the physical spatial constraint of the sphenoid sinus. Specifically, the diameter of the coil needs to be large enough - larger than the pituitary - such that the pituitary is in the region of high sensitivity. The diameter also needs to be large enough to achieve sensitivity at a depth of the farthest point of the pituitary because the optimal coil diameter is proportional to the imaging depth of interest: $R_{optimal} = \frac{d_{max}}{\sqrt{5}}$, where d_{max} is the maximum distance of interest from the coil [16]. Endonasal placement requires that the coil be able to bend slightly beyond a U-shape in order to pass by the nostril. In 20 consecutive endoscopic pituitary surgeries, various sizes of sterile cotton patties ("cottonoids") were subjectively assessed by author MB. The experience revealed that a coil diameter up to 2.5-cm could easily be inserted without hyperangulation (kinking). Once past the nostril, further advancement into the sphenoid sinus was easy and safe.

3.2 Coil and Interface Design

The coil (Fig. 2.1) consisted of a 20 mm inner diameter loop made from a single continuous copper trace (3 mm in width and 17.8 μm in thickness) on a flexible printed circuit board (PCB). A coaxial cable (Siemens Healthineers, Forchheim, Germany: 50 Ω, 1.13 mm diameter, 0.22 mm inner conductor diameter, 20 cm length) connected the coil to a custom 3D printed circuit box located outside the body. This box housed the electrical pre-amplifier circuit, with adjustable components needed for tune and match. All of the electronics can be kept outside the body with only the coil loop and cable needing to be inserted endonasally. The coil assembly was tuned to

a resonance frequency of 123.2 MHz (for 3T imaging), and impedance matched by adjusting the electrical components contained in the box [17]. The circuit was also designed to actively decouple the loop, without lumped element capacitors, during the transmit portion of the pulse sequence. The active detuning was accomplished by putting an inductor in parallel with the net capacitance of the coax cable during the transmit portion of the pulse sequence, detuning the inductive coil loop. Due to proprietary Siemens hardware, a custom built-in docking port was designed specifically for our assembly by author RH via an MCX connector.

3.3 Coil Performance Simulation

Modeling of the MRI RF coils is an important step in coil design and development. A 3D coil model was developed in COMSOL® (COMSOLAB, Stockholm, Sweden) to study the magnetic field distributions of the coil. A circular loop coil with a 20 mm inner diameter and a trace width of 3 mm was set up in the frequency domain. The coil was assigned as Perfect Electric Conductor surface, and the current flowing in the coil was set to 1 A. The sample properties in the simulation were set up according to the material properties of the agar-carrageenan gel [18]. For this finite element simulation, a maximum element size of 0.5 mm was used on the region of interest (ROI), and the simulated fields from the coil, $\boldsymbol{B_1}$ fields, at each vertex were imported into MATLAB (The MathWorks, Inc., Natick, Massachusetts, United States) for post-processing.

The simulated amplitude of the effective transverse field $B_{1xy\,effective}$ at the resonance frequency within the ROI was evaluated and then compared with the MRI scan results. The magnetic field components were simulated with the coil plane

parallel to the B_0 field (θ = 0°) (Fig. 3.1a), and then the amplitude of the effective transverse field at a certain rotation angle θ (0°< θ ≤ 90°) with respect to B_0 (Fig. 2b) was derived as:

$$B_{1y\,effective} = B_{1y} \cdot cos\theta - B_{1z} \cdot sin\theta \qquad (1)$$

$$B_{1xy\,effective} = \sqrt{B_{1x}B_{1x}^{\ *} + B_{1y\,effective}B_{1y\,effective}^{\ *}} \qquad (2)$$

where B_{1x}, B_{1y}, and B_{1z} are the magnetic field components for our RF receiving coil in x, y, z directions at θ = 0°. B_{1x}, B_{1y}, and B_{1z} remain constant during the rotation.

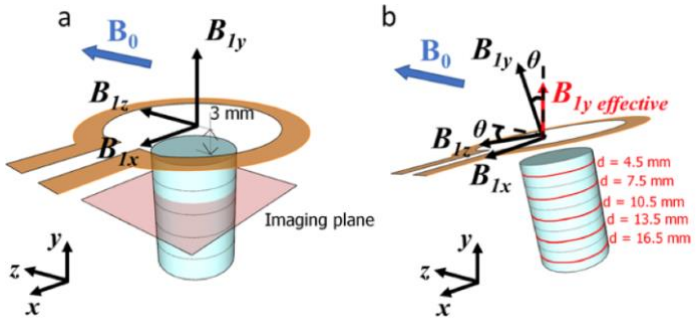

Figure 3.1: *Schematic diagram of the miniature coil. The blue cylinders represent the region of interest (ROI) at various distances d from the coil.* $\boldsymbol{B_0}$ *is in the +z axis. A: The coil resides in the x-z plane at* $\theta = 0°$*. B: The coil is rotated around the x-axis at an angle,* θ*, where:* $0° < \theta \leq 90°$*.*

3.4 Phantom Design and Construction

A 3D-printed phantom was designed and manufactured to roughly mimic the sphenoid sinus dimensions as an igloo-shaped configuration (Fig. 3.2a and 3.2b). A surrounding cylindrical jar (Fig. 3.2d) allowed for easy rotation of the assembly, effectively tilting the coil rotation angle relative to the B_0 field.

To assess imaging resolution, the five holes, ranging from 1 mm to 2.8 mm in diameter, were drilled into an acrylic plate (2.5 cm thick and 7.5 cm wide), which was attached under the igloo cavity (Fig. 3.2c). In addition, a center hole of 12.7 mm in

diameter was drilled to provide sufficient volume for SNR measurements. The cavity and the resolution plate were then fixed inside a transparent cylindrical plastic jar, parallel to the jar wall (Fig. 3.2d and 3.2e). The plastic jar was chosen to have a similar size as a human head, 13 cm in diameter and 12 cm in height. The plastic jar was rested on a pair of 3D-printed supporters, so the jar was able to be rotated and set at the desired scan angle. The plastic jar, including the holes in the resolution plate, was filled with agar gel, which consists of distilled water, 1% agar powder, 2% Kappa carrageenan, and 22 μmol/kg of gadolinium contrast (Fig. 3.2f) [19]. A portable vector network analyzer (VNA) was used to tune and match the coil after placing the coil inside the igloo cavity of the phantom (Fig. 3.3a).

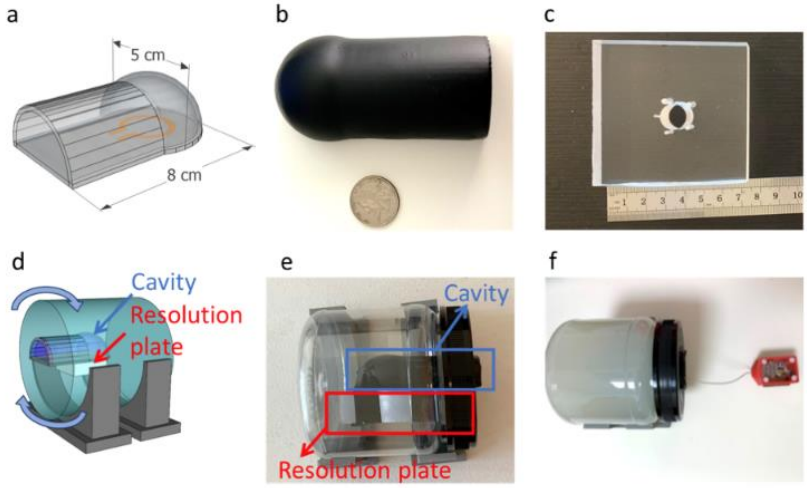

Figure 3.2: *Experimental setup, including the igloo cavity, resolution plate, and agar phantom. An igloo cavity holds the coil and is sealed to hold only air, mimicking the sinus cavity. A resolution plate is placed directly on the outside of the igloo cavity to measure the SNR at the location where the pituitary gland would be. Outside of the igloo is surrounded by agar gel to act as a phantom a: CAD model of the igloo cavity. The coil was placed inside the cavity. b: The 3D-printed igloo cavity. The cavity was waterproofed with the Plasti Dip (Plasti Dip Int., Minneapolis, MN, USA). A U.S. quarter is shown for reference. c: The resolution plate with hole diameters 1 mm, 1.6 mm, 2 mm, 2.4 mm, 2.8 mm, and 12.7 mm. The smaller holes were used for visual demonstration and the 12.7 mm hole was used for SNR calculation. d: CAD model of the phantom set up. The cavity was fixed inside a plastic jar and then placed on two 3D-printed supporters, allowing the jar to be set to the desired coil angle. e: Assembled phantom set up. The resolution plate was taped tightly under the cavity and then the cavity was fixed in a plastic jar. f: The plastic jar was filled with agar gel, and the coil was placed inside the cavity.*

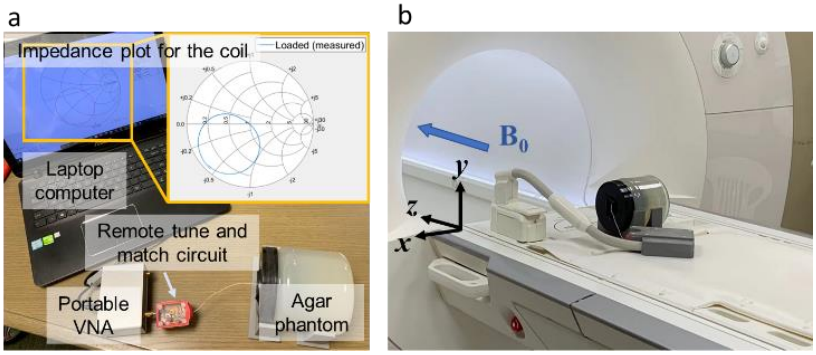

Figure 3.3. *The tune and match process and the MRI scan experiment set up. a) A portable vector network analyzer (DG8SAQ VNWA 3, SDR-Kits, United Kingdom) was used for tune and match analysis after placing the coil inside the agar phantom. b) The tune and match box was connected to the pre-amplifier, and MRI scans were performed on the phantom.*

3.5 MRI Studies Using the Phantom

The tune and match of the miniature coil were performed by measuring the frequency response using the portable VNA for loaded and unloaded cases. Loaded S11 is measured with the phantom placed under the coil while unloaded S11 is measured with no phantom presented. For both loaded and unloaded cases, the miniature coil was tuned and matched to the resonance frequency of 123.2 MHz.

The T1/T2 value of the agar phantom was measured to be 1250/64 ms, with T1/T2 map sequences [20]. Standard resolution proton density Turbo Spin Echo (SD PD-TSE) sequences (Table 1) were used to compare our miniature coil with the commercial Siemens 20-channel HeadNeck coil, both quantitatively and qualitatively. Here we chose proton density because it is a direct measure of the maximum signal. The 2D SD PD-TSE sequence was scanned at 10 different coil rotation angles, ranging from 0 ° to 90°.

Given the expected higher SNR, we scanned the miniature coil with a 2D high-resolution proton density Turbo Spin Echo (HD PD-TSE) sequence (Table 1) at 0° and 60° coil angles. Images were reconstructed from the frequency data directly via inverse Fast Fourier Transform (iFFT). The HD PD-TSE scan was also performed on the commercial head coil using the same scan sequence. The commercial head coil images were sum-of-square combined after coil reduction.

Table 3.1: *The parameters for High-Resolution 2D PD-weighted TSE sequence and Standard-Resolution 2D PD-TSE sequence*

	SD PD-TSE	HD PD-TSE
Echo time (ms)	9.1	14
Repetition time (ms)	3000	3000
Refocusing angle (degree)	160	160
Bandwidth (Hz/pixel)	250	250
Acquisition matrix size	320×320×15	320×320×35
Field of view (mm^3)	220×220×45	64×64×25
Resolution (mm^3)	0.7×0.7×3	0.2×0.2×0.7
Phase over sampling	0%	100%
Scan time (mm:ss)	03:09	06:21
Parallel imaging	No	No

3.6 SNR Computation

For each angle, SNR measurements for the single-channel custom coil were calculated from two repeated standard-resolution 2D PD-TSE scans. The region of interest (ROI) was divided into five cylindrical slices - each with 1 cm diameter and 3 mm thickness (Fig. 2) - inside the resolution plate center hole under the coil (Fig. 3d and 3e). When combined, the slices form a 1 cm diameter region 3 mm to 18 mm away from the miniature coil. The defined ROI has a size comparable to a typical pituitary gland [21].

SNR measurements were calculated with methods described by Constantinides et al. for magnitude images of a single-coil array [22]. SNR was calculated as the ratio of signal and noise ($SNR = S / \sigma$). The signals were measured as the mean intensity within the ROI:

$$S = \frac{1}{N_{ROI}} \sum_{i=1}^{N_{ROI}} A_{ROI_i} \qquad (3)$$

Where N is the number of samples and A is the pixel intensity. The noise was measured as the background standard deviation on a signal-free region:

$$\sigma = \sqrt{\frac{1}{N_n}\sum_{i=1}^{N_n}\left(A_{n_i} - \overline{A_{n_i}}\right)^2} \quad (4)$$

In this experiment, the signal-free region was selected within the acrylic plastic part of the resolution block.

For the 20-channel commercial head coil, the SNR was calculated based on Kellman's method for root-sum-of-squares magnitude combining images, which is the gold standard for multi-channel phased array coils [23]. The scaled noise covariance matrix was calculated by averaging pixel SNR within ROI from two repeated standard-resolution 2D PD-TSE scans. Standard-resolution proton density Turbo Spin Echo (PD-TSE) MRI scans (Table 3.1 line 1) were performed on the phantom for SNR measurements for both miniature flexible coil and commercial head coil, and a coil simulation model was developed to characterize the performance of the coil. We plotted the SNR maps and the amplitudes of the simulated effective transverse B_1 field distributions for θ from 0° to 90°, at defined ROIs from 4.5 mm to 16.5 mm distance to the coil, shown in Fig. 3.1.

3.7 S11 Comparison

The reflection coefficient S11 was recorded and then compared with the simulated S11 for the loaded and unloaded cases (Fig. 3.4). The simulated S11 generally agrees with the measured S11. The quality factor Q-factor can be approximated as the ratio of the resonant frequency (f_0) to the 3dB bandwidth (Δf_{3dB}) [24]. The simulated quality factors for the loaded case and the unloaded case are found to be Q_{loaded}^{sim}= 16.88, $Q_{unloaded}^{sim}$= 308. And the measured quality factors are Q_{loaded}^{mea}= 11.18, $Q_{unloaded}^{mea}$ = 36.29. The lower Q-factors from the measurement are likely to be the

result of the environment loss that was not included in the simulation. A common measure for sensitivity to loading is the ratio between the unloaded Q-factor and loaded Q-factor [25], [26]. The measured Q-ratio is found to be Q_{ratio}^{mea} = 3.25 and the simulated Q-ratio is Q_{ratio}^{sim} = 18.25. A Q-ratio that is larger than 2 indicates that the sample noise dominates the coil noise [11].

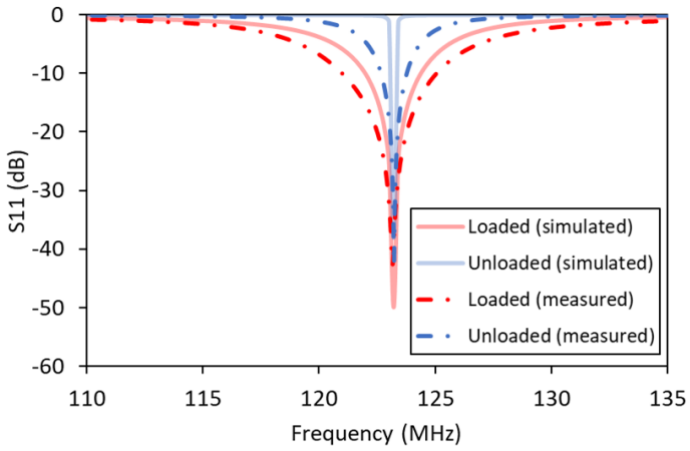

Figure 3.4: *Comparison of S11 with and without the load measured with the VNA and simulated using COMSOL. The coil in both loaded and unloaded cases was tuned and matched to the resonance frequency.*

3.8 In-plane SNR map

Phantom scan in-plane SNR maps are shown in Fig. 3.5. The imaging planes were selected parallel to the coil surface at 4.5 mm and 10.5 mm below the coil, as a zoom-in shot on the resolution plate. The amplitudes of the simulated effective transverse B_1 field distributions at the same coil depth distance and rotation angles as the SNR maps are also shown in Fig. 6. In the simulation, the in-plane effective field amplitudes were normalized based on the maximum $B_{1xy\,effective}$ field at 4.5 mm below the coil.

As the coil angle increases, the overall SNR and the amplitude of the $B_{1xy\,effective}$ within the ROI decreases. Because of the circular shape of the small

coil, the magnetic field from the coil is not uniform, and dead spots, where $B_{1xy\,effective}$ drops to zero, were observed in the in-plane results. When the rotation angles increased from 0° to 90°, the dead spot gradually moved from the edge of the ROI to the center of the ROI in both experiment and simulation. The simulated field distributions qualitatively matched with the scan experiment SNR maps.

A comparison of the high-resolution PD-TSE image between the head coil image and the miniature coil images is shown in Fig. 3.6. Though the SNR decreases with increasing rotation angle, the phantom signal is still uniform at 60° coil angle, and the image SNR is high enough to clearly show the 1 mm hole on the resolution plate.

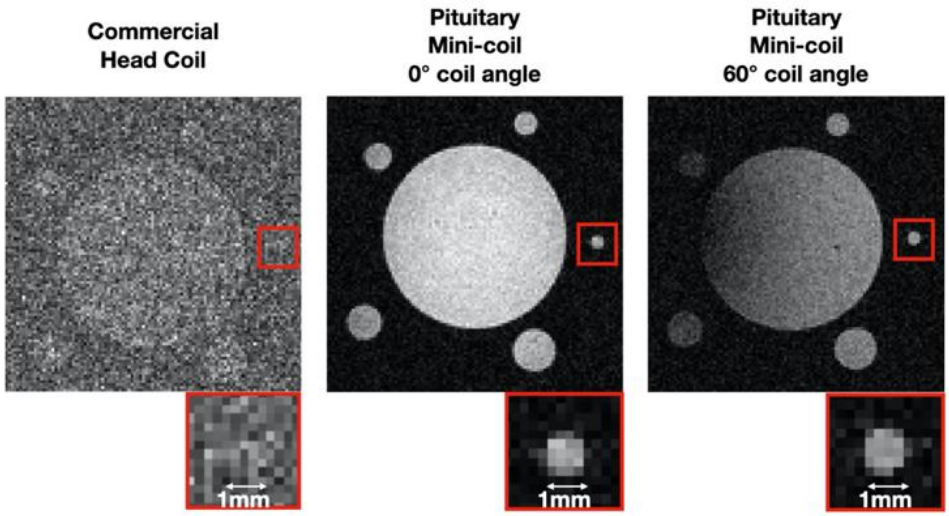

Figure 3.6: *High-resolution PD-TSE image comparisons, using the commercial head coil (left), and the pituitary miniature flexible coil at θ = 0° (middle) and θ = 60° (right). The voxel size is 0.2 × 0.2 × 0.7 mm^3. Imaging planes were selected 1 cm from the coil. Images from miniature flexible coil are at the same window level, while the image from the commercial head coil is at its own window level for better visualization.*

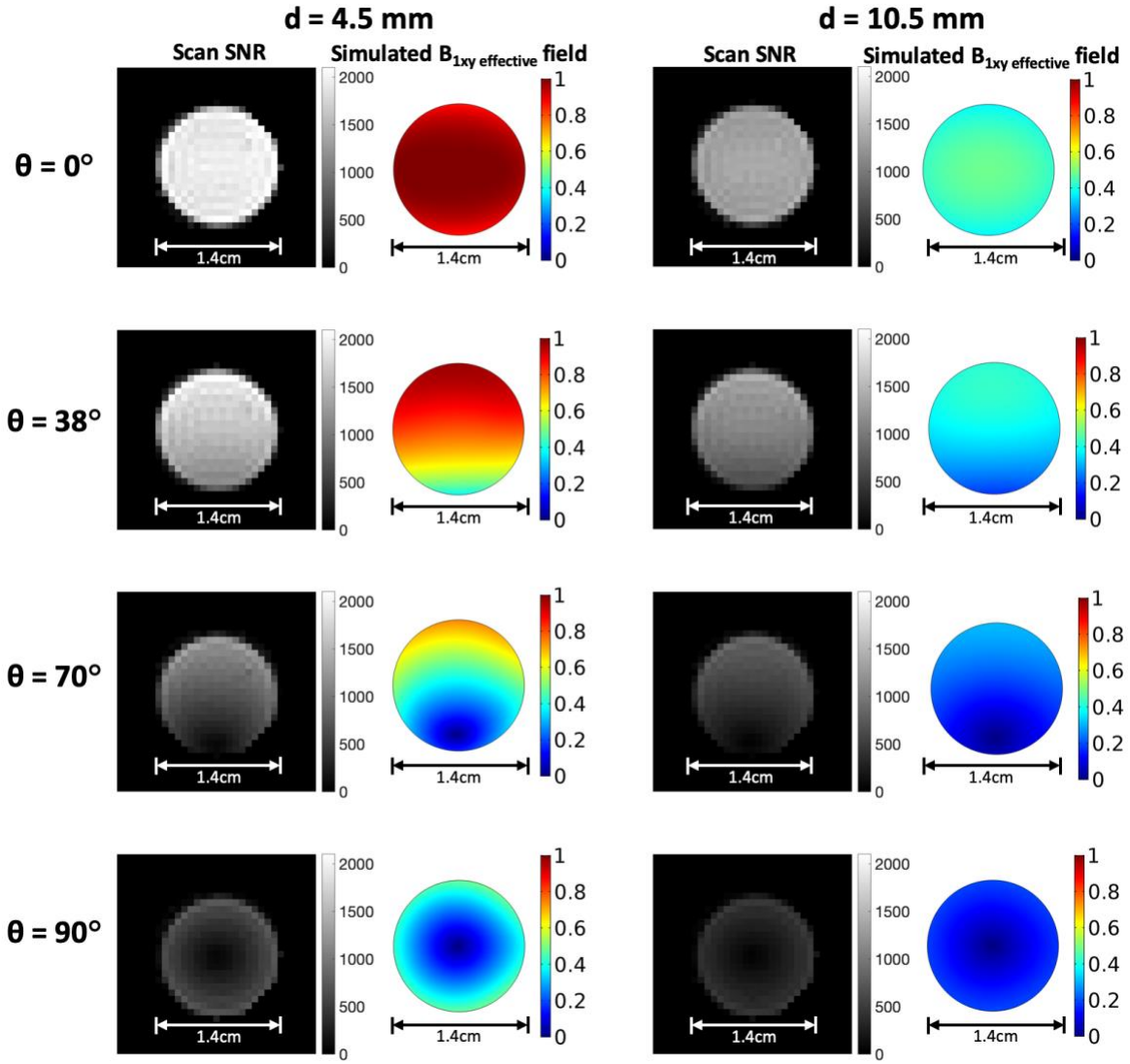

Figure 3.5: *The scan (Table 1 line 1) signal SNR maps and normalized amplitude of the simulated effective transverse B_1 field distributions at θ = 0°, 38°, 70° and 90°, respectively. d indicates the distance between the coil and the imaging plane. The imaging planes were selected to be parallel to the coil plane. Column 1&3: The SNR maps at the respective coil distances d and rotation angles θ. Column 2&4: The amplitudes of the simulated effective transverse B_1 field distributions at the central hole on the resolution Linear color scale indicates the level of the SNR and the normalized $B_{1xy\,effective}$. The simulation fields were normalized based on the maximum $B_{1xy\,effective}$ field at d = 4.5 mm.*

3.9 Mean SNR vs. Coil Distance & Rotation Angle

The mean SNR of the ROI from the phantom scan with respect to distance from the coil and the rotation angles are shown in Fig. 3.7, and then compared with the normalized mean $B_{1xy\,effective}$ within the ROI from the simulation. We normalized the effective transverse field predicted by simulation at a single point (θ = 0° at 4.5 mm below the coil). By setting this one point equal to the experimentally measured SNR, we can see that the simulations of magnetic field amplitude track with the experimentally measured SNR, with an error of 1.1% ± 0.8%. The mean effective field at θ = 90° dropped to around 20% of the mean-field found at θ = 0° for all ROI depths. At θ = 0°, the mean effective field at 16.5 mm slice was 23.1% of the mean effective field at 4.5 mm slice. For an ideal coil, at θ = 90°, the coil magnetic field B_1 is parallel to the main field B_0, and the SNR is expected to drop to zero. However, in the real case, only the B_{1y} component of the coil field is parallel to B_0 at θ = 90° (Fig. 3.1b), and spins can still be excited by B_{1x} and B_{1z} components, providing a reduced but detectable signal. The mean SNR of the 20-channel commercial head coil based on Kellman's method was 99.5 (Fig. 3.7) [23], which was uniform across the ROI.

A Bland-Altman plot of two repeated standard-resolution PD-TSE scans, as shown in Fig. 3.8 was generated to show the inter-scan SNR consistencies. The 95% confidence interval indicated majority of repeated scans are within ±5% difference, which demonstrated the consistency and the repeatability of measure SNRs from phantom scans.

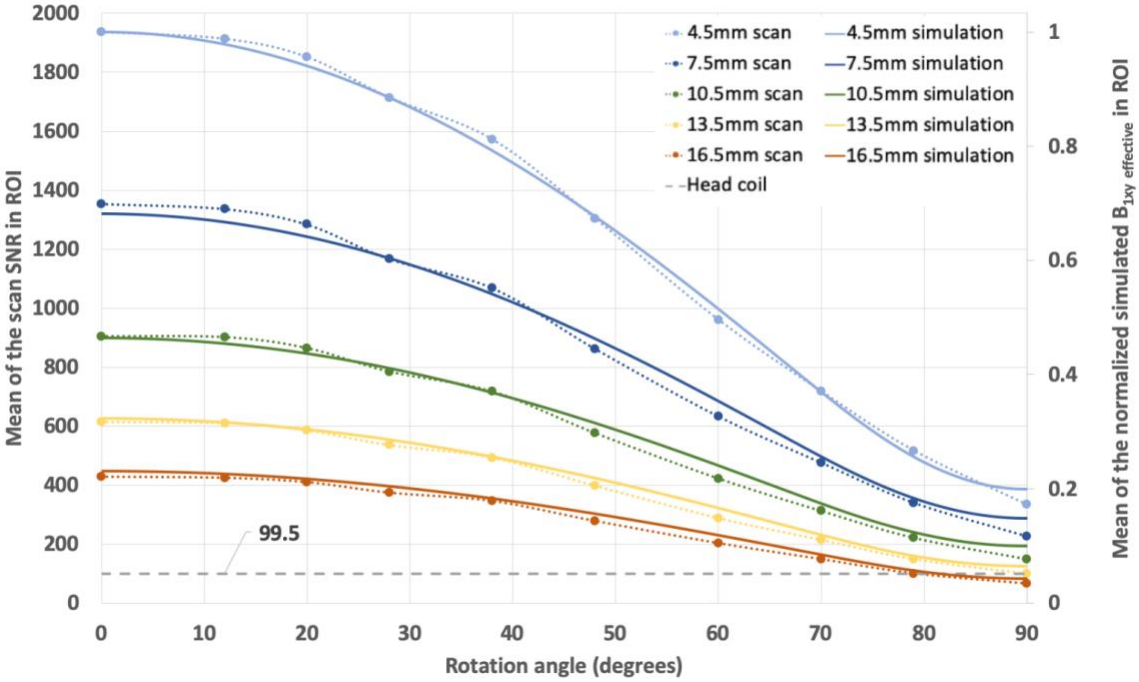

Figure 3.7: *Mean SNR from the scan at various ROI depths and rotation angles, compared with the corresponding mean of the normalized effective transverse B_1 field from the simulation. The simulated fields were normalized to a single point, the mean $B_{1xy\,effective}$ at $\theta = 0°$ at 4.5 mm below the coil.*

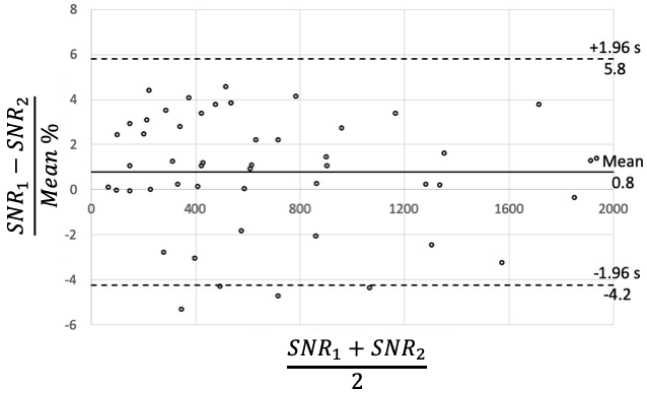

Figure 3.8: *Bland-Altman plot for SNR of two repeated SD PD-TSE scans, SNR_1 and SNR_2. X-axis is the mean of the two scans, and Y-axis is the percentage difference.*

3.10 Discussion

Our prototype coil, which was specifically designed for intra-operative imaging of the pituitary gland, achieved up to a 19-fold SNR improvement compared to a commercial head coil in this agar phantom study. Our "worst-case-scenario," a rotation angle of 60 degrees and an ROI depth of 16.5 mm, still produced a 2-fold relative increase in SNR. Re-tuning or matching is not necessary after the coil placement since the coil is tuned and matched after being placed in the sphenoid sinus. Since the coax cable is 20 cm long, it is short enough not to pick up any significant currents from the body coil during Tx. If the coax cable is made to be longer than 20 cm, common mode current chokes could be placed along the length of the cable to impede the shield currents. This technique is supplemented with a balun on the pre-amplifier circuit board.

The increased SNR from the miniature coil enabled a markedly higher resolution imaging compared to the commercial head coil. The voxel size of the high-resolution sequence is approximately 1/50th of the standard-resolution. Because the SNR is proportional to the voxel size [27], our coil enabled a much-increased spatial resolution of that currently used with standard 3T imaging. At this reduced voxel size, the inadequate SNR associated with the commercial coil was demonstrable. To the contrary, our phantom study suggests that pituitary adenomas of 1 mm and smaller may be detectable using our custom miniature intrasphenoidal coil.

Multiple aspects of the electromagnetic behavior and performance of our custom coil were accurately simulated using a COMSOL multiphysics approach. The simulation of the effective magnetic field aligns with the experimentally measured SNR across a clinically relevant range of coil angles and distance, both in-plane pixel-wise and through-plane. The consistency of these two groups of simulation data and experiment data

validates both the numerical simulation model and SNR experiments. The SNR from repeated scans also had little difference, demonstrating precise SNR measurements. The discrepancy remaining between the mean SNR curve and the simulation curve is likely attributable to errors in the imaging plane alignment. The imaging planes were selected manually on the scanner, and any mismatches in distance or rotation angle can create shifts in the SNR curves. Validated with the phantom scan experiment, this coil simulation model is important in studying the interaction between the RF fields from the surface coil and the ROI or the phantom.

An additional advantage of our design approach, which is modular and relatively easily adaptable, is that in theory the same relative multiplicative improvements in SNR would be achievable with higher field MRI scanners as they become clinically available. Prior research has qualitatively examined the image quality improvement for pituitary MRI with 7T scanners [3], [10]. Since a real-time tune and match is performed, the coil can be tuned to other resonance frequencies and thus suitable for any MRI scanner.

Chapter 4: Clinical Application Study

4.1 Surgical Placement

An example hypothetical miniature coil surgical placement with the simulated SNR improvements in pituitary region is as shown in Fig.4.1. In the zoom-in view of the sphenoid sinus and the pituitary, the 2.6 cm miniature coil could be placed at a 30° angle with respect to B_0 field. Both coil placement and pituitary gland contour were drawn by an experienced neurosurgeon. The gradient line plots overlay represents the SNR improvement factors of our coil compared to the commercial head coil, which were estimated based on the mean SNR from the scan of the miniature coil and the commercial head coil. In this case, the pituitary gland enjoys a 12 to 19 times of SNR improvement at the region close to the coil, and at least 3 times of SNR improvement at the region further away.

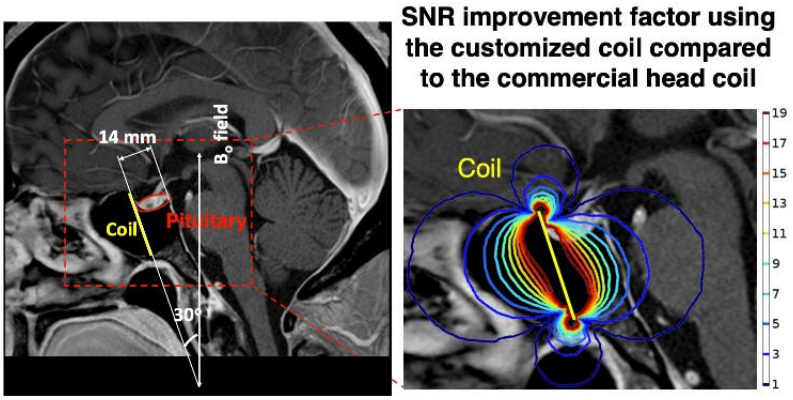

Figure 4.1: *Coil surgical placement example on the retrospective patient image. SNR improvement using the miniature coil compared to a commercial head coil was estimated using the simulated effective field at θ = 30°. The red ellipse indicates the location of the pituitary gland.*

4.2 Sphenoid Sinus Measurements

MPRAGE brain MRI sequences of 50 patients without sellar tumors were included in this analysis. Images from a 3T MRI (Siemens Prisma, Siemens Healthineers, Erlangen, Germany) 3D magnetization prepared radiofrequency pulse rapid gradient echo T1 with and without gadolinium (Gd-DTPA, 0.1 mmol/kg) contrast were downloaded from the PACS server and subsequently de-identified. Using axial slices, the maximum lateral intrercarotid distance and maximum distance at sellar face were measured. Using midline sagittal slices, craniocaudal sphenoid distance anterior to the sella, distance from coil to the posterior pituitary gland, and craniocaudal sellar distance were measured.

50 patients with available MP RAGE brain MR imaging without sellar tumors or prior sinus surgery underwent measurement of sphenoid sinus parameters. On midline sagittal images (Fig. 4.2a) the average craniocaudal sphenoid distance anterior to the sella was 24 ± 4 mm. The average distance from the planned coil placement to the posterior pituitary gland was 13 ± 2 mm. The average craniocaudal sellar distance was 7 ± 2 mm. On axial images (Fig. 4.2b), the average maximum lateral inter-carotid distance was 27 ± 3 mm. The average maximum distance at the sellar face was 16 ± 4 mm. The distributions of the primary measurements, craniocaudal sellar distance at 0, 20, and 30 degrees of angulation and lateral intercarotid distance, were greater than 20 mm (Fig. 4.2c). For placement at 0° angle of the B0 static field, the craniocaudal distance (24 ± 4 mm) was the limiting constraint. We chose one standard deviation at the lesser dimension as the basis for subsequent simulation experiments and the use of the 20 mm flexible transnasal

coil. As shown below, slight angulations up to 20° angle did not significantly degrade the coil SNR performance, and therefore we anticipate this size coil could be used in nearly every patient.

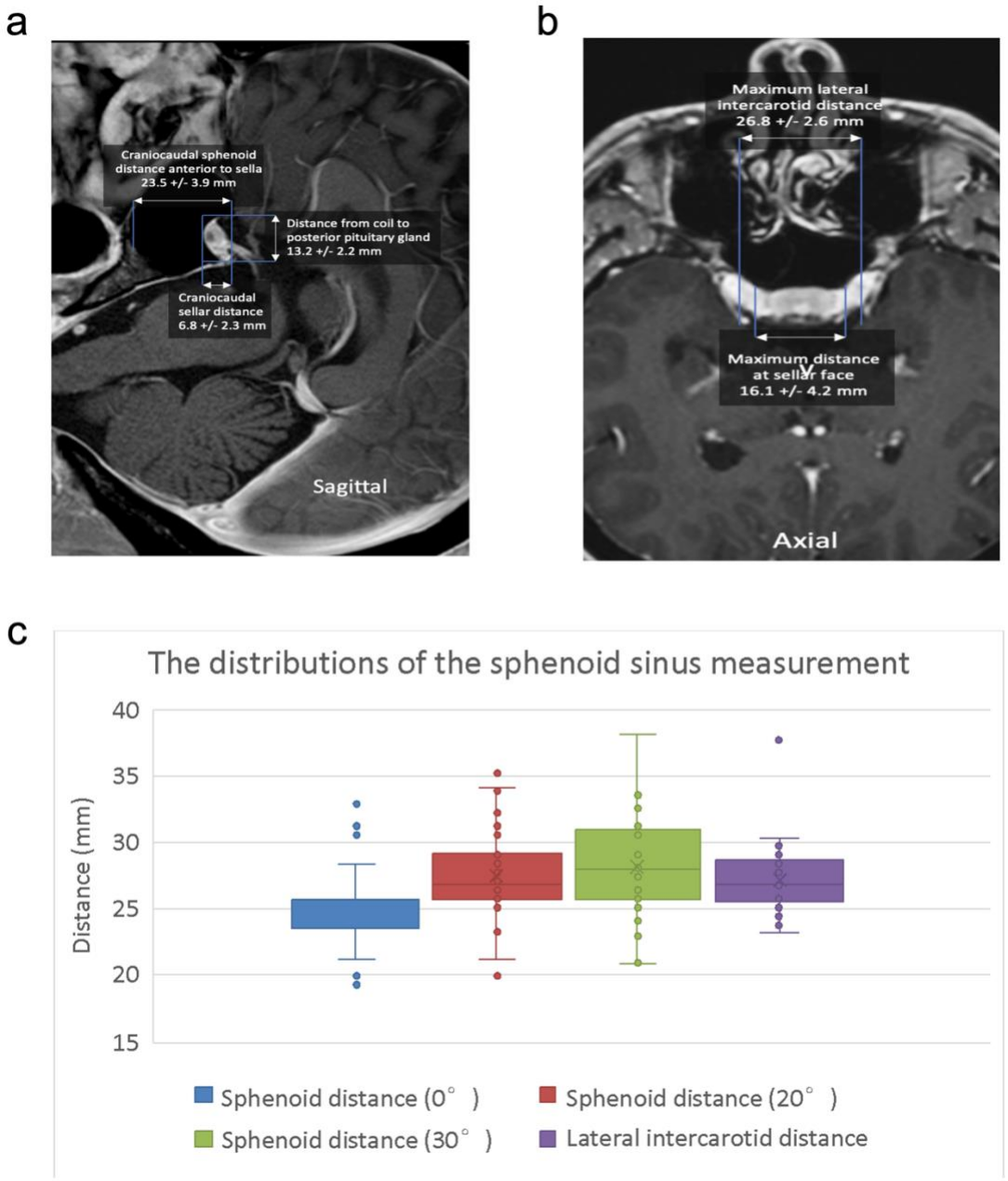

Figure 4.2: *Anatomic measurements of the sphenoid sinus in 50 patients using magnetic resonance imaging T1 with contrast images in the midline sagittal (a) and axial (b) planes. The distributions of the craniocaudal sphenoid distance at various degrees and the lateral intercarotid distance (c).*

SNR improvement of the transnasal coil compared to the commercial Siemens 20-channel Head/Neck radiofrequency coil was simulated. The effective transverse field B_{1xy} of the coil was simulated at a 0°, 20°, and 30° coil rotation angle in the sella. Gradient contour plots spatially represent the SNR improvement from use of the miniature coil (Fig. 4.3). For a 0° rotation angle (where the coil plane is parallel to the MR scanner headrest), a 20-fold SNR improvement was expected inside an area measuring 6.0 mm × 17.0 mm around the coil and a 10-fold SNR improvement was expected inside an area measuring 15.2 mm × 17.5 mm. With coil rotation, there was a decrease in the height of the improved SNR region, but an increase in the width. Simulations with a coil placed at a 20° rotation angle yielded an expected 20-fold SNR improvement in an area measuring 5.8 mm × 18.5 mm around the coil and a 10-fold SNR improvement in an area measuring 15.0 mm × 19.5 mm around the coil. Simulations with a coil placed at a 30° rotation angle yielded an expected 20-fold SNR improvement in an area measuring 5.0 mm × 19.5 mm around the coil and a 10-fold SNR improvement in an area measuring 14.3 mm × 20.0 mm around the coil. As shown in the simulation, the transnasal coil is predicted to improve the SNR by 12 to 20 times compared to the commercial head coil at the region close to the coil, and at least 4 times of SNR improvement at the region further away.

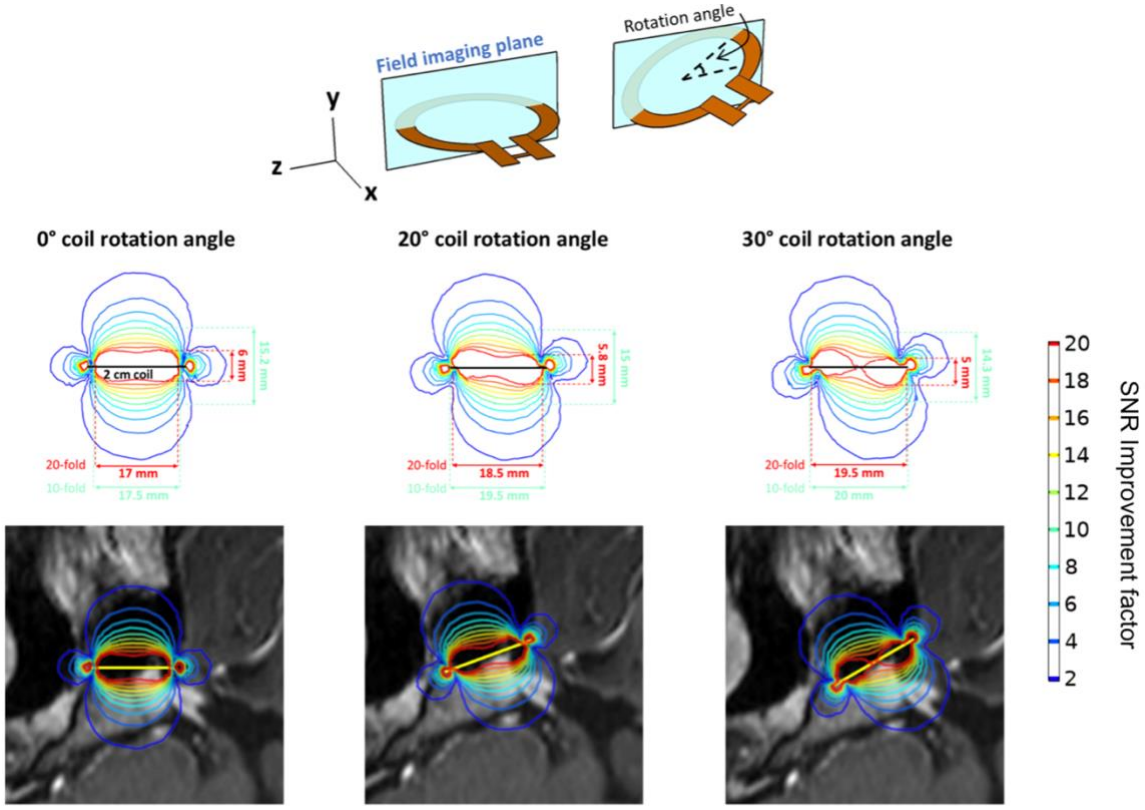

Figure 4.3: *Electromagnetic simulations with a 2 cm radiofrequency coil predicting signal-to-noise ratio increases at various distances from the coil and with various coil rotation angles relative to the horizontal MRI head holder and superposition of these simulations on an MRI T1 with contrast sphenoid sinus region.*

4.3 Cadaveric Studies

4.3.1 Coil Design Iterations for Cadaveric Studies

Based on the sphenoid sinus measurements, 2-cm diameter is the ideal size for the miniature flexible coil to fit 95% of the patients. A 2-cm diameter loop defining the radiofrequency coil was made from a single continuous copper trace (2 mm in width and 17.8 mm in thickness) and attached to a coaxial cable (Siemens Healthineers: 50Ω, 1.13 mm diameter, 0.22 mm inner conductor diameter, 20 cm length). There were no electrical components directly on the coil, and the tune-and-match components were placed at the end of the 20 cm coil outside the body. The 20-cm cable is short enough avoid any significant current from the body coil during the transmission, while a longer cable would require common mode current chokes along the length of the cable in order to impede the shield current. The coil component was coated with Plasti Dip (Plasti Dip Int., Minneapolis, MN, USA) to prevent fluid electrical coupling and for future planned sterilization. This coating was conformal and flexible (Fig 4.4).

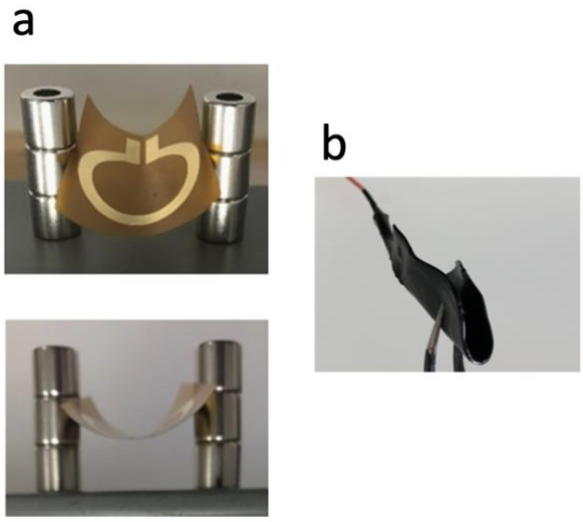

Figure 4.4: *(a) The coil was designed with flexibility for transnasal application and (b) a protective coating was applied to the coil to maintain this flexibility.*

4.3.2 Cadaveric Studies Setup

Three cadaveric human heads were used to simulate flexible miniature coil placement. A standard endonasal endoscopic approach was carried out to gain unobstructed access to the sella [*Figure 3D*]. Any sphenoid septations were drilled down. Bone over the sella was not removed. The coil was inserted through a single nare under endoscopic visualization and positioned directly over the sella parallel to the floor [*Figure 3F*] with the cadaver head facing towards the ceiling. A bovine collagen sponge (HeliSTAT, Integra LifeSciences Corporation, Plainsboro, NJ) [*Figure 3E; 3G*] was placed in the clival recess and over the coil to limit air-bone interface and associated artifact. The coil wire was secured to the external nare with a 3-0 vicryl suture and adhesive. The cadaveric specimen was then transported to the MRI scanner and examined again to confirm that detachment and movement had not occurred during transport.

The prepared cadavers with transnasal coils in place were scanned with Siemens Prisma 3T MRI Scanner via the T1-MPRAGE sequence and Proton Density sequence at varying resolutions (T1: 0.9 mm × 0.9 mm × 0.9 mm; 0.4 mm × 0.4 mm × 0.4 mm; 0.2 mm × 0.2 mm × 0.2 mm (transnasal coil only); PD: 0.7 mm × 0.7 mm × 3 mm; 0.2mm × 0.2 mm × 0.7 mm) [*Supplementary Tables 1-2*]. T1-MPRAGE sequence is commonly used clinically, while the Proton Density sequence was performed for pixel SNR measurement. For the head coil, the phase oversampling was enabled to avoid phase wrapping artifacts due to the small field of view. Phase oversampling was unnecessary with the transnasal coil given localized signal. The pituitary gland was segmented into four 3mm regions (a, b, c) defined by proximity to the sella. Segmentation was performed by two independent observers (S.L., K.P.). Signal was found within each region, noise was defined as the standard deviation of the background intensity, and the SNR was

calculated as the signal intensity divided by the noise. The mean SNRs within the pituitary gland were calculated for the segmented regions of interest from the high-resolution proton density sequence images and were compared between head coil and transnasal coil.

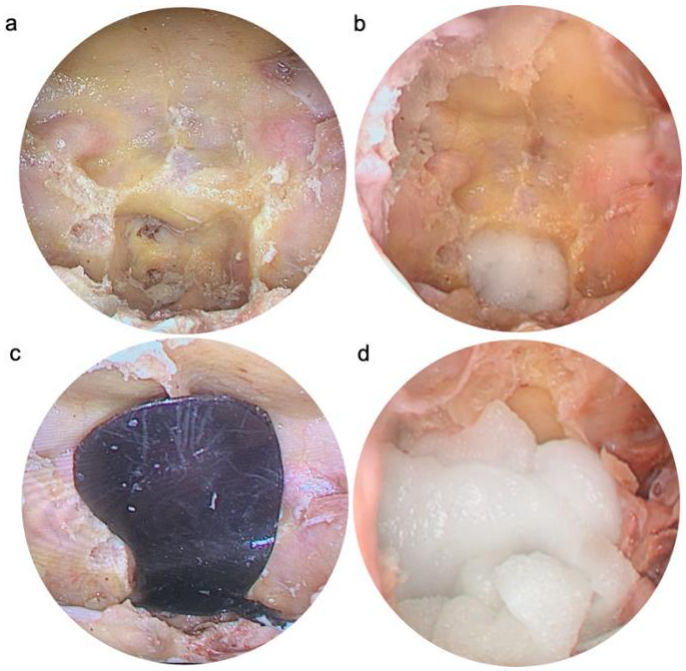

Figure 4.5: *(a) Cadaveric preparation of the sella with the removal of sphenoid septae and mucosa, (b) placement of collagen sponge in clival recess to eliminate air-bone interface artifact, (c) placement of exible mini coil at 0 degrees, (d) filling of the sphenoid sinus with collagen sponge.*

4.3.3 Visual and SNR Improvements with Flexible Coil in Cadaveric Studies

Cadaver heads containing the flexible coil were imaged to compare differences in SNR. The sellar region was also imaged with the clinical Head/Neck coil MP-RAGE sequences with 0.9 mm slice thickness (Fig. 4.6A) and 0.4 mm slice thickness (Fig 4.6B). The transnasal coil shows significantly improved resolution of the pituitary soft tissue as compared to the head coil (Fig 4.6C).

SNR calculations were calculated for various regions of interest (ROI) (Fig 4.6D) The mean SNR for the most anterior region (Region a) was 48.5 and the furthest region (Region c) was 14.9 (Table 4.1). The mean SNR for the entire pituitary gland ROI (Region a+b) was 39.0. The mean SNR for the head coil was 2.3 and was uniform across the all ROIs. The flexible coil demonstrated a maximum of 21-fold mean SNR improvement and

an average of 17-fold mean SNR improvement of the pituitary gland compared to the commercial head coil (Table 4.1).

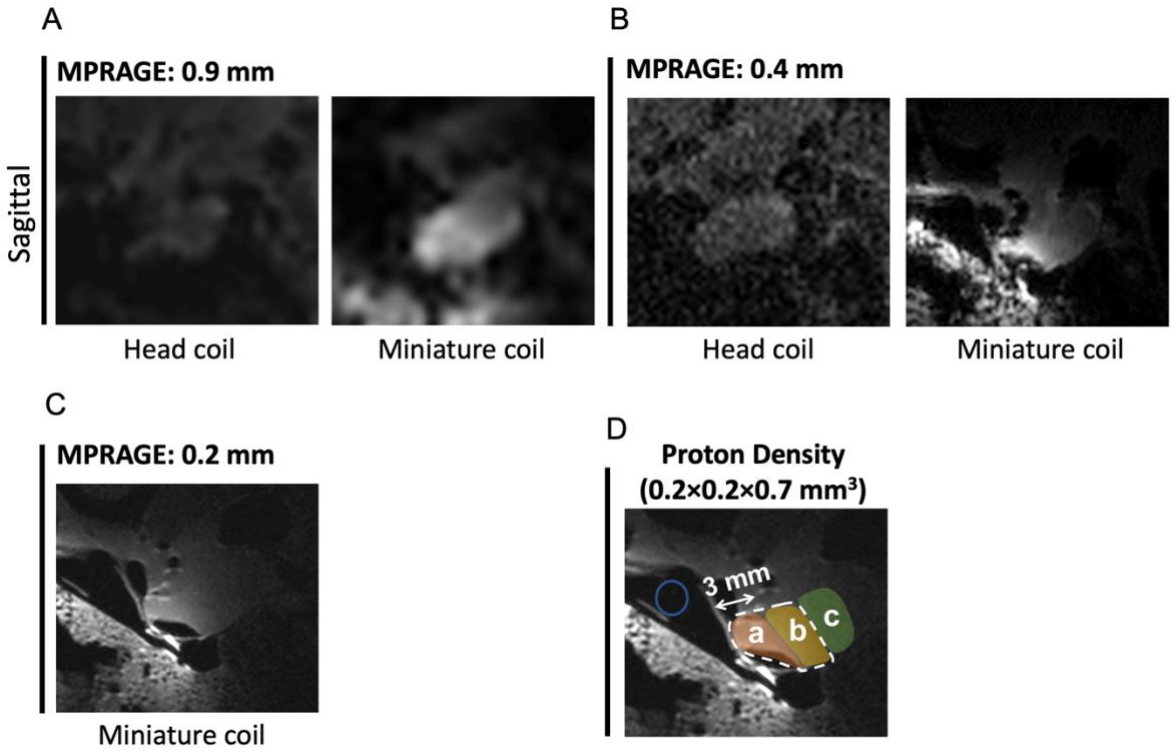

Figure 4.6: *Cadaver heads with the placement of the flexible coil on T1-MPRAGE images with 0.9 mm slice thickness (A), 0.4 mm slice thickness (B), and 0.2mm slice thickness (C). The images were compared with the images from the Siemens 20-channel Head/Neck coil at the same resolutions. The pituitary gland region of interest (marked by white dotted circle) was divided into 4 sub-regions with 3 mm width: Region a, Region b, Region c, and Region d (D). The noise region of interest is identified by the blue circle.*

Table 4.1: *Mean SNR comparison for high-resolution MRI (Proton Density: 0.2×0.2×0.7 mm³)*

Table 1 – Mean SNR comparison for high-resolution MRI (Proton Density: 0.2×0.2×0.7 mm³)			
ROI	Transnasal coil	Head coil	Improvement factor
ROI a	48.5	2.3	21.1
ROI b	29.4		12.8
Pituitary gland (ROIs a and b)	39.0		17.0
ROI c	14.9		6.5

4.3.4 Histological Correlation

In a single cadaver head, flexible coil images identified a hypointensity not identified on images using the standard head coil [Figure 5A-B]. Following imaging, the pituitary was removed en bloc, sectioned in the coronal plane, para31n embedded and stained with hemotoxylin and eosin as well as reticulin. [Figure 5C-D]. A board-certi31ed pathologist identi31ed a pituitary cyst on histological sections that potentially correlated with imaging ndings, although left/right directionality was lost on tissue acquisition and processing.

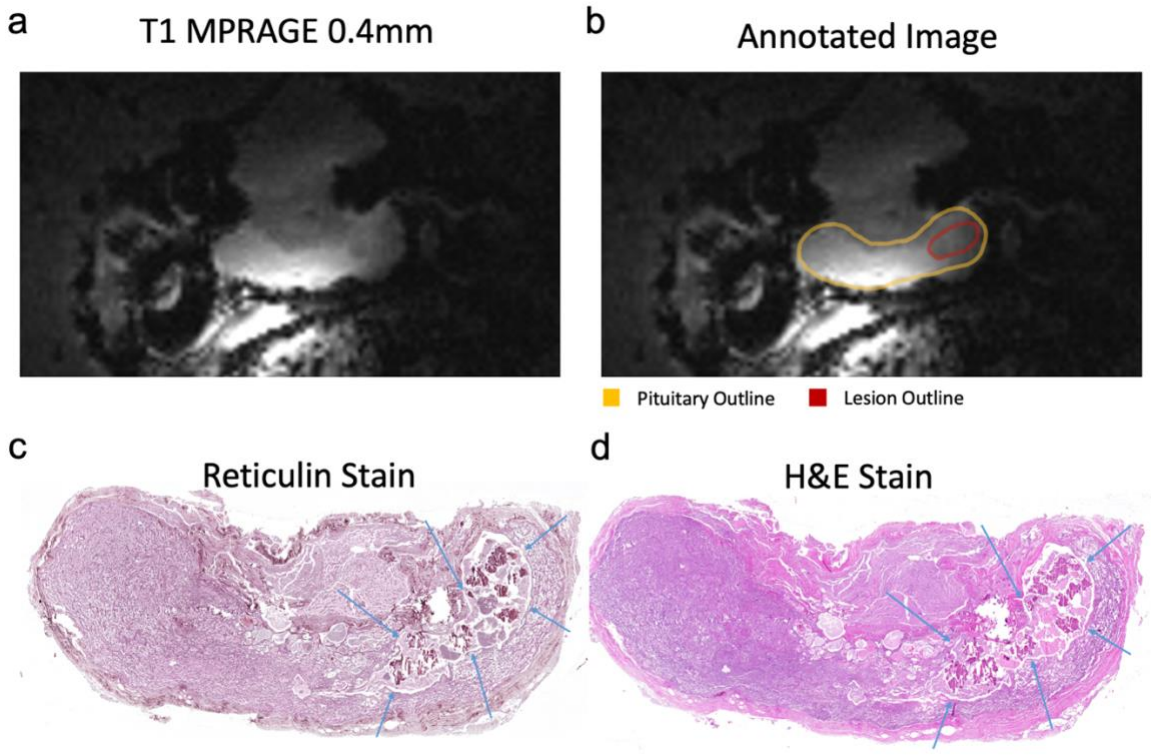

Figure 4.7: *(a) A coronal view of the pituitary gland using high-resolution Proton density (0.2mm x 0.2mm x 0.7mm) image with the flexible coil in a cadaveric specimen, (b) the annotated image showing highlighted pituitary gland (yellow outline) and hypointensity (red outline). (c, d) Corresponding coronal sections with reticulin stain and H&E stain show a cyst like structure in the lateral aspect of this gland.*

4.3.5 Temperature Measurements

To assess for safety, the flexible coil was tested for radiofrequency heating by inserting it into a 980 gram pork meat phantom within a room maintained at 20°C. The temperature measurements were performed with a benchtop fiber optic thermometer (FOTEMP1-4, Optocon®). The probe was positioned at two different positions inside the meat phantom. One probe was placed right beneath the coil (measuring site S1) and the other one was on the coil trace (measuring site S2). A continuous 15-minute fast low angle shot three-dimensional imaging (FL3D) sequence was performed on the meat phantom during the temperature measurement (TR = 20 ms, TE = 5 ms, FA = 5°). The body coil was used as the transmit coil and the time-averaged RF power was 0.3 W.

With the 2-cm coil in direct contact with the phantom (Fig. 4.8a-b), the change in temperature during a 15-minute scan was measured to evaluate for safety. With a 0.3 W time-averaged RF power, there was no detectable change in temperature throughout the experiment at two measurement sites [0° change at site 1; 0° change at site 2, Fig. 4.8c].

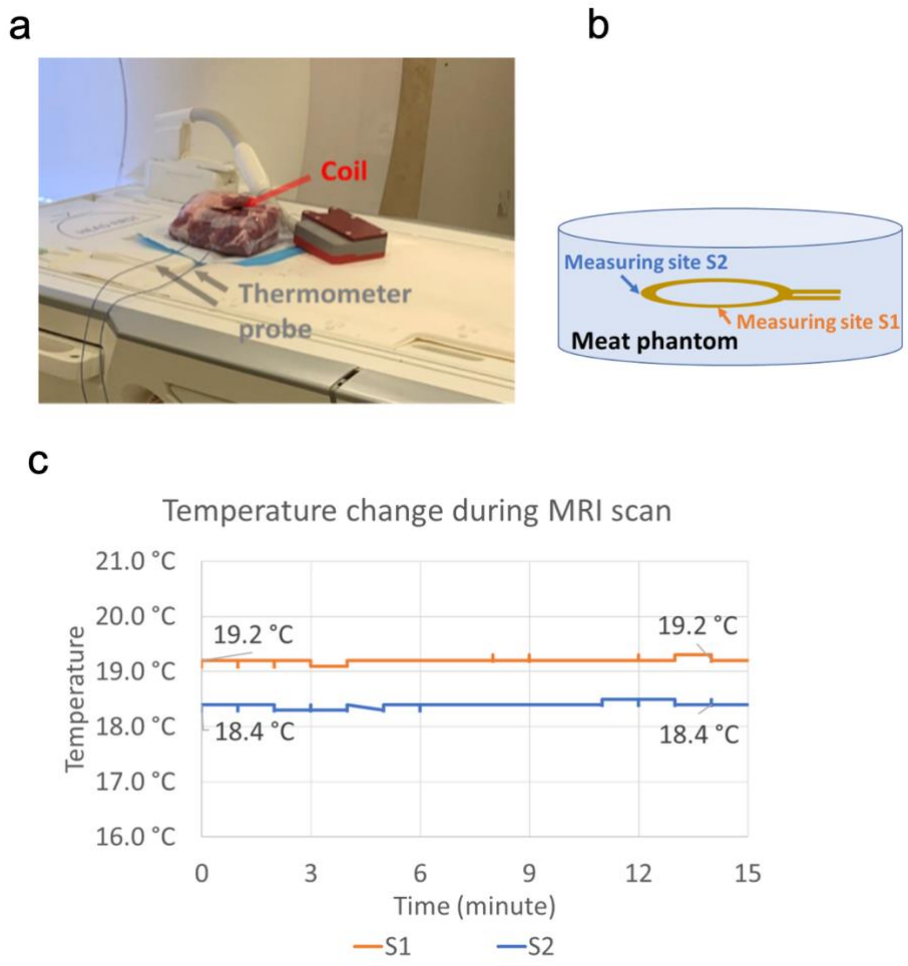

Figure 4.8: *(a) Meat phantom with direct coil placement and thermometer placement and (b) schematic illustrations of the two temperature measuring sites. (c) Temperature recordings at measuring sites S1 and S2 for the 15-minute fast low angle shot three-dimensional imaging (FL3D) sequence scan.*

4.4 Discussions

We show the development, feasibility, and SNR improvement of a flexible coil for imaging of the pituitary gland. Establishing a range of anatomic sphenoid sinus measurements in the general population allowed for the implementation of a 2 cm coil that can be applied to 95% of patients. A coil electromagnetic simulation model was used to predict the SNR improvement of using a flexible coil compared to a commercial head coil, providing a convenient and time-efficient way to characterize the coil performance in the clinical environment. Moreover, the simulation model can also be useful in selecting the optimal coil size and shape based on the specific anatomy of each patient in future clinical studies.

The safety and feasibility of the coil placement were evaluated for potential clinical use. During the 15-minute scan, no detectable temperature change was found. The average specific energy absorption rate (SAR) during the scan can be estimated by dividing the time-average input RF power by the sample mass [28]. Therefore, the experimental average SAR is well below the guideline value [29]. We demonstrate that the flexible coil is unlikely to cause thermal damage to the patient and is safe to be used in the clinical environment. In addition, pre-clinical insertion of the coil in a cadaver head was carried out with the subsequent demonstration of 17-fold increased SNR of the pituitary gland in this model. Lastly, we identify a cadaveric case where flexible coil 1) identified potential lesion that was not detected on standard head coil and 2) potentially correlated with histologic abnormality. We hypothesize this technique may be applicable to small functioning pituitary tumors.

There is limited published data using this strategy. Chittiboina et al. [13], published a cadaveric study using a 12 mm flexible coil inserted using a microscope-based sublabial

approach and imaging performed using a 1.5T scanner. The coil was inserted through the retractor system, and the tip ended up between 4.2 and 17 mm from the pituitary gland. In approximately half of the cases where the coil was in close proximity to the sella there was a mean 10-fold SNR improvement, while the other half of the cases showed an improvement of less than 5-fold. In comparison, our study uses a larger flexible coil placed along the sella through an endonasal endoscopic approach without the need for a custom securing apparatus and with complete visualization both before and after coil placement. Overall, we utilize a similar strategy of image improvement with potentially increased SNR improvements with the more contemporary endonasal endoscopic approach for pituitary surgery.

Of note, the MRI quality in cadaveric tissue is known to be different from clinical images, and therefore the overall image quality is reduced from clinical standards. Despite this known limitation of our study, we demonstrate a difference in SNR between the head coil and flexible coil, as well as an expected improvement with better spatial resolutions in each coil. In addition, our pathological analysis is limited in that left/right orientation could not be preserved with fixation and staining. Despite this, we found a potential pathological correlate in the pituitary sample with a hypointensity seen on the flexible coil MRI and may serve as a proof of concept of identification of pituitary lesions not seen on standard MRI. Overall, these data demonstrate that the flexible coil can likely be safely used in a clinical setting and has the potential to identify pituitary tumors that are missed on standard clinical MRI sequences. Further research will investigate the safety and feasibility of the flexible coil in patients undergoing surgery for functional ACTH-producing pituitary tumors with negative imaging.

Chapter 5: Conclusions

A miniature flexible coil has been developed, and its feasibility was validated using numerical simulations and experimental phantom. The proposed coil design can be surgically positioned in close proximity to the pituitary gland, which can provide a maximum of 19-fold SNR improvement compared to a commercial head coil within a region of interest in the agar phantom study. A 3D coil simulation model was cross-validated with the experimental scan results, where the simulation model can be used to develop and refine new coil designs with predicted SNR gains in future studies.

The clinical study describes a transnasally-placed 2-cm flexible coil to improve the resolution of pituitary imaging. The coil is compatible in 95% of patients, can be successfully placed in contact with the sella in cadaver studies, shows no temperature changes in phantom studies during scanning, and improves the SNR of the pituitary by an order of 17. This study provides feasibility data for the promise of application to the clinical setting to improve detection of small ACTH-secreting pituitary tumors when clinical pituitary MRI fails.

Chapter 6: Future Work

A novel miniature flexible coil that can be placed within millimeters of the pituitary gland was developed, to drastically improve the SNR and image quality of the gland. While the clinical application studies in this work provided surgical feasibilities, there are several major areas that can be further studied to enable in-vivo experiments.

Surgical Coil Placements and Protocols

While the simulated coil placement results demonstrated that the flexible coil can fit 95% of the patients, this statistical finding is a retrospective imaging study, and it is not confirmed in cadaveric studies. A large cadaveric study with the standard clinical transnasal endoscopic procedure is necessary to verify the percentage of the patients whom the flexible coil can fit with an ideal scanning coil angle.

In cadaveric studies, physicians use HeliSTAT to fixate the coil angle and positions. This may be sufficient for cadaveric studies as there are no patient motions. A better technique and protocol should be developed to better fix the coil positions, as the coil angle is crucial for imaging performances.

Motion Correction

This study only considered stationary objects as phantoms and cadaver heads. Respiratory motion and cardiac-synchronized brain motion during the in-vivo MRI is a well-documented problem [30]. Motion compensation techniques in pulse sequence and image reconstructions should be applied to mitigate the motion corruption artifacts. Respiratory motion is one of the main sources of imaging artifacts, which severely impair image quality and clinical diagnosis. A common solution is breath-holding, which requires fast scanning time with a highly accelerated pulse. Imaging sequences such as single-shot turbo-spin echo (SSTSE), and balanced steady-state free precession (bSSFP), can reduce

the scan time to a single breath-hold time [31]. Another solution is free-breathing continuous scanning with motion correction image reconstruction algorithms [32], [33]. Cardiac-synchronized brain motion can cause sub-millimeter displacements and induce blurry motion artifacts, which hinders the detection of microadenomas [8]. ECG-gated or self-gated MRI sequences can effectively mitigate the cardiac motion artifacts [34], [35]. Motion correction reconstruction with slice-to-volume registration is another direction to mitigate the motion artifacts in image reconstruction and post-processing. Multiple sets of scans from three orientations are registered onto a single high-resolution 3D volume iteratively, with a motion-robust reconstruction [36].

Image Quality and Microadenomas Detectability Study

In one cadaver study, we found a potential pathological correlate in the pituitary sample with a hypointensity seen on the transnasal coil MRI, our pathological analysis is limited in that left/right orientation could not be preserved with fixation and staining. A large cadaveric study with more rigorous pathological assessment cross-validation is necessary to demonstrate the detectability of microadenomas of the flexible coil.

While the cadaver scan images show significant image resolution improvement over the commercial head coil, the MRI quality in cadaveric tissue is known to be different from clinical images, and therefore, the overall image quality is reduced from clinical standards. The actual SNR and image resolution improvements in in-vivo surgical applications need further verification.

High-Resolution 3D MRI with Deep Generative Networks via Novel Slice-Profile Transformation Super-Resolution

Chapter 7: Introduction and Motivation

7.1 Introduction

Spin-echo-based acquisitions, such as turbo spin-echo (TSE) or fast spin-echo (FSE) imaging, are preferred for clinical magnetic resonance imaging (MRI) image interpretation for high spatial and contrast resolution for the detection of pathology [37] Three-dimensional (3D) TSE imaging is limited by its long imaging time and related blur image artifact associated with patient motion [38]–[40] Instead, multi-slice two-dimensional (2D) TSE imaging is the standard for a range of clinical applications due to its spin-echo-based acquisitions with high contrast and high in-plane resolution (e.g., 0.3-1 mm). However, a stack of 2D slices in a multi-slice 2D acquisition typically has a thicker through-plane resolution (e.g., 3-6 mm), yielding low-resolution (LR) multi-planar reformation (MPR) with staircase artifact due to elongated voxels [40], [41]. As a result, multiple stacks of 2D TSE scans are often acquired in multiple orthogonal imaging planes (e.g., axial, coronal, and sagittal planes), and in some applications, up to five imaging planes (axial, coronal, sagittal and two oblique planes) [41]–[43]. These approaches increase the overall scan time, decrease patient comfort, and can also limit the streamlined interpretation of images (e.g., radiologists may need to draw a region of interest (ROI) separately on multiple 2D scans from different orientations). Therefore, methods that achieve super-resolution (SR) transformation of a single multi-slice 2D TSE scan into a high-resolution (HR) isotropic 3D MRI will be valuable to reduce overall imaging time and improve the interpretation of TSE-based MRI images.

Super-resolution reconstruction (SRR) with slice-to-volume registration (SVR) methods have been established to reconstruct a single 3D SR volume from multiple 2D MRI scans[43]–[47] Slice-profile downsampling has been proposed to transform SR volume back to LR 2D volumes for fidelity constraints. These SVR algorithms are iterative and require multiple 2D MRI scans, thus increasing the acquisition time and reconstruction time. In contrast, deep-learning-based super-resolution (SR) showed promises in SR of 3D MRI or in-plane 2D MRI [48]–[60]. However, applying them to through-plane 2D MRI is non-trivial because of the imperfect slice-selection profile[61].

In this work, we propose a novel slice-profile transformation super-resolution (SPTSR) framework. The SPTSR framework enables the application of deep learning super-resolution to a single stack of multi-slice 2D TSE MRI to achieve 3D isotropic super-resolution by using training inputs synthesized by a realistic representation of the low-resolution through-plane images and slice-profile-transformation based inference pipeline. As multiple orthogonal imaging planes are commonly used in clinical multi-slice 2D TSE MRI, we apply slice-profile-transformation based downsampling (SP-DS) to multi-slice 2D coronal TSE scans as training input to the deep generative model and test our proposed generative network on multi-slice 2D axial TSE scans, reformatted to the coronal plane. We use multi-slice 2D T2-weighted (T2w) prostate MRI, and our aim is to achieve super-resolution 3D imaging with an isotropic resolution of $(0.625\text{mm})^3$ from a single multi-slice 2D T2w MRI scan of 3.6mm slice spacing. In addition, we simulated 2D T2w MRI with a large dataset of 3D T2w MRI scans to quantitatively evaluate SPTSR with ground-truth images.

The main contributions of our SPTSR framework include that

1) We used a dedicated observation model (i.e., an appropriate definition of a 2D

excitation profile) that enables coronal (or axial) scans for supervised training via SP-downsampling to perform SR of axial (or coronal) scans.

2) Both the training and inference images are blurred via SP-downsampling and SP-conv to match the slice profile kernel in the two orthogonal directions, and the output images are then deblurred via SP-deconv to achieve super-resolved isotropic 3D imaging.

3) The purpose and necessity of SP-downsampling, SP-conv, and SP-deconv, collectively referred to as SPTSR, are proved both in theory and experimental results.

4) With extensive visual, qualitative, and quantitative comparisons, we establish that SPTSR significantly improves the quality of SR images when compared to the SMORE method [62] and k-space zero-fill (KS-ZF) trained networks.

5) The feasibility of using only one multi-slice 2D TSE scan for a high-resolution MPR is shown using the SPTSR framework. This can potentially save total MRI scan time considerably as it negates the necessity of scanning multiple stacks of 2D TSE scans in orthogonal imaging planes.

7.2 Related Works

Existing super-resolution reconstruction (SSR) methods generally require multiple 2D MRI scans to iteratively register and reconstruct a single 3D SR volume. Greenspan et al. proposed an inter-slice super-resolution algorithm that utilized three stacks of multi-slice 2D images, each volume shifted by a sub-pixel amount in the slice direction [63]. An iterative back-projection algorithm was used to reconstruct the high-resolution image volume [63]. Rousseau et al. and Jiang et al. developed slice-to-volume registration (SVR) to register multiple sets of scans from three orientations onto a single high-resolution 3D volume [44], [45]. Gholipour et al. used a total of scans from three orientations to perform

SVR and iterative SSR [46], [47]. They proposed a slice acquisition model, including SP-downsampling, which was used to iteratively transform the SR volume back to LR input volume, and enforce the fidelity constraints [46], [47]. For lengthy cardiac cine scans, motion-compensated reconstruction was proposed to combine multiple 2D cine scans into a 3D cine volume [64]. Automated pipelines with CNN-based initial SVR estimation and CNN-based localization and segmentations were also developed [36], [43], but iterative SSR was still performed. SSR frameworks demonstrated qualitative and quantitative improvement from the 2D scans [65], [66]. However, these SSR approaches used multiple 2D scans and iterative SSR algorithms, which significantly increased the acquisition time and the reconstruction time.

Deep learning SR algorithms are the state-of-the-art for SR in natural images and have become increasingly popular for SR in MRI [55], [67]. Many studies focused on SR of 3D MRI or in-plane SR for 2D MRI and showed promise in achieving high in-plane resolution with single-image SR [48]–[60]. To synthesize the LR training input from the HR reference images, these works used either averaging-based or interpolation-based downsampling [48]–[54] or KS-ZF downsampling [55]–[60]. However, applying them to achieve high through-plane resolution is challenging with multi-slice 2D TSE imaging datasets because super-resolution algorithms were trained and tested along with the frequency and phase encoding directions. Frequency and phase encoding schemes divide the voxels evenly in the frequency domain, where they are continuous, uniform, and non-overlapping [68]. In this case, training input for super-resolution can be easily synthesized by downsampling HR reference images. In contrast, multi-slice 2D TSE imaging is realized by applying a radiofrequency (RF)-excitation pulse with a slice-selection profile for each individual slice [61]. Due to MR hardware limitations, the slice-selection profiles may not

be sharp-edged and can overlap with adjacent slices [61]. To compensate, slice spacing greater than the slice thickness is often used to avoid the slice overlapping, resulting in physical discrepancies between the evenly-spaced super-resolution and through-plane resolution of multi-slice 2D TSE imaging. Training input for super-resolution cannot be easily synthesized by simple downsampling due to the fundamental difference between actual through-plane resolution and synthesized low-resolution images.

Several studies have proposed to increase the through-plane resolution of multi-slice 2D MRI with learning-based super-resolution. Jurek et al. developed a CNN-based super-resolution reconstruction using thick slices [69], and Zhang et al. developed a GAN-based super-resolution algorithm with multiple 2D scans [70]. Bhatia et al. proposed SR of cardiac MRI with coupled dictionary learning [71]. These three methods all generate the LR simulated input with averaging-based or interpolation-based downsampling. While they show impressive with simulated testing data, they did not perform testing on actual 2D scans. Sood et al. [41], [72] used training from conventional k-space zero-filled downsampled HR axial prostate MRI to test on reformatted multi-slice 2D coronal MRI. Although excellent validation results were shown, the testing results did not fully resolve the staircase artifact and were visibly much noisier compared to the reference images. SMORE is the state-of-the-art SR algorithm that super-resolves one stack of 2D slices to an isotropic 3D volume [62]. SMORE trained on downsampled HR axial slices and infer on the reformatted 2D coronal slices. It attempted to factor in staircase artifacts by applying a self-supervised anti-aliasing step (SAA) but did not fully consider slice profiles during the downsampling and inference. Thus, although it demonstrated good results in brain MRI, certain anatomically challenging MRI scans may not be applicable due to the limitations of the training data. Our proposed SPTSR will be extensively compared with SMORE as the

state-of-the-art.

Chapter 8: Slice-profile Transformation Super-resolution (SPTSR) Framework

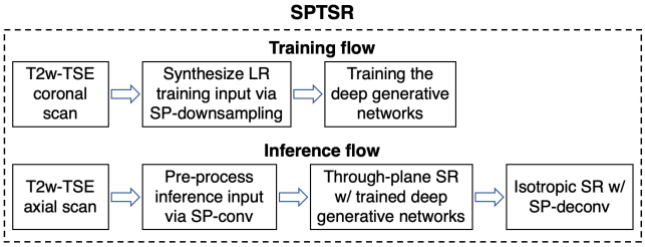

Figure 8.1: *The overall SPTSR framework, with training flow (top) and inference flow (bottom).*

We describe the complete framework of our proposed SPTSR in detail, summarized in Fig. 8.1. Current clinical MRI scans, including prostate, brain, and placenta MRI, commonly include several stacks of multi-slice 2D TSE MRI scans with two or three orthogonal orientations (e.g., axial, coronal, and sagittal) to compensate for low through-plane resolution. The goal of the proposed SPTSR framework is to train from one orientation of a single stack of 2D slices (e.g., a coronal MRI scan) and use the orthogonal orientation (e.g., an axial MRI scan) to infer an isotropic high-resolution 3D imaging volume. The isotropic 3D imaging volume can be transformed into other orientations via MPR. For this to work:

- We designed a novel slice-profile transformation super-resolution (SPTSR) framework, with a pre-processing SP-downsampling for an orthogonal stack of multi-slice 2D scan as the training input, a pre-processing SP-conv for the inference input, and a post-processing SP-deconv for the inference output.
- We utilized a large clinical prostate MRI dataset, consisting of axial and coronal stacks of multi-slice 2D TSE MRI scans, for training, validation, and testing.
- We designed the WGAN-GP scheme for the training of our deep generative networks.

8.1 Slice-Profile Transformation

We define a stack of multi-slice 2D coronal images as I_{cor} (with high resolution in the SI-direction) and a stack of multi-slice 2D axial images as I_{ax} (with low resolution in the SI-direction). A set of I_{cor} is used for training and validation, and $I_{ax\to cor}$, reformatted from axial to coronal planes is used for the input to the inference model. Although not shown, the principle would hold the same way for other orientations (e.g., $I_{ax\to sag}$, $I_{cor\to ax}$, etc.). We define V as the underlying isotropic high-resolution 3D imaging volume with a matrix size of $N_{LR} \times N_{AP} \times N_{SI}$ and field-of-view (FOV) of $F_{LR} \times F_{AP} \times F_{SI}$.Then, I_{cor} and I_{ax} at the pixel/slice indices, x, y, z, with the same FOV are expressed as:

$$I_{cor}(x,y,z)|_{x\in[1,\,N_{LR}],y\in[1,NS_{AP}],z\in[1,N_{SI}]} = \sum_{j=y\times DS_{AP}-\left\lfloor\frac{L}{2}-1\right\rfloor}^{j=y\times DS_{AP}+\left\lfloor\frac{L}{2}\right\rfloor} PSF_{AP}(j)V(x,j,z), \quad (1)$$

$$I_{ax}(x,y,z)|_{x\in[1,N_{LR}],y\in[1,N_{AP}],z\in[1,NS_{SI}]} = \sum_{k=z\times DS_{SI}-\left\lfloor\frac{L}{2}-1\right\rfloor}^{k=z\times DS_{SI}+\left\lfloor\frac{L}{2}\right\rfloor} PSF_{SI}(k)V(x,y,k), \quad (2)$$

where PSF_* is the normalized one-dimensional (1D) slice profile for a given RF-excitation pulse, NS_* is the number of slices, and DS_* is the spacing between slices in coronal ($*$=AP) and axial ($*$=SI) scans. L is the slice thickness, full-width-half-max (FWHM) of PSF. DS_x becomes same as L if there is no slice gap. j, k are upsampled indices to account for non-integer indices after scaling. The PSF is approximated as truncated sinc function. While the true slice profile is possible to compute by the combination of slice profiles of RF excitation and refocusing pulses, the difference between exact and approximated ones

would be subtle and beyond the scope of our work as we apply projection to all signals.

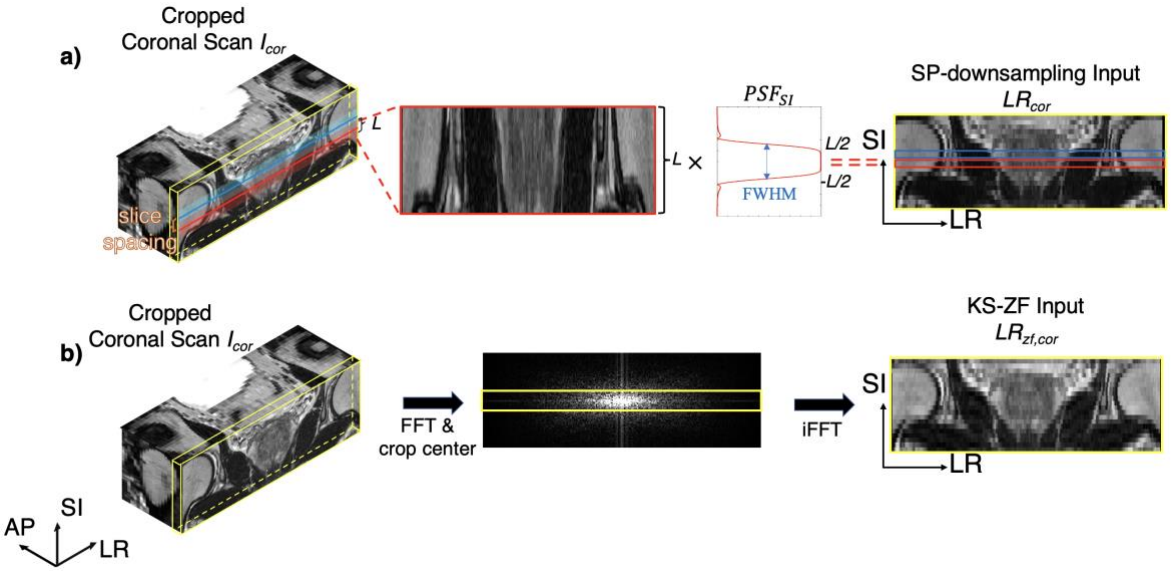

Figure 8.2: *a) The proposed SP-downsampling method. Each line of pixels is acquired by multiplying the slice profile PSF_{SI} of length L, to the same physical location on the cropped coronal scan; b) The KS-ZF downsampling method. Each slice of image is transformed to the frequency domain via FFT, cropped its center lines and iFFT back to the downsampled image.*

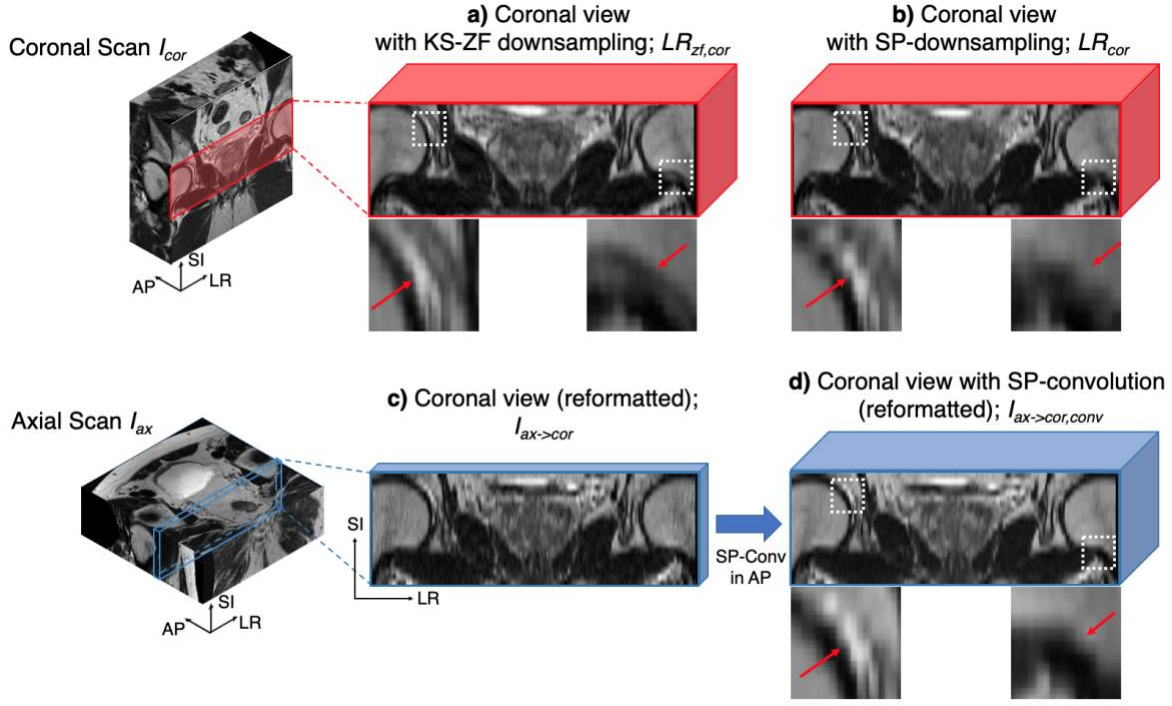

Figure 8.3: *The down-sampling method visual comparison. a) the conventional KS-ZF downsampled image patch, b) the SP-downsampled image patch, c) the reformatted axial patch, and d) the SP-convolved axial patch. Thickness in each patch represents the voxel thickness in the AP-direction. All patches are bilinear interpolated to demonstrate the visual differences.*

Previous studies attempted to synthesize $I_{ax\rightarrow cor}$ by downsampling I_{cor} via k-space zero-filling (KS-ZF)) [21]–[24]. The KS-ZF transforms the source image to the frequency domain via FFT, crops the center at 1/up-sampling factor, and converts it back to the image domain via iFFT, as illustrated in Fig. 7.2b. Essentially, the KS-ZF in the axial plane $LR_{zf,cor}$ can be expressed as applying a 1D-lowpass filter with a rectangular window to I_{cor} in the SI-direction:

$$LR_{zf,cor} = LP_{SI}(I_{cor}), \qquad (3)$$

where LP_{SI} is the 1D low-pass filtering along the SI-direction. $LR_{zf,cor}$ and I_{cor} form the conventional LR-HR training pair for KS-ZF trained deep learning networks. However, $LR_{zf,cor}$ is inherently different from its reformatted version from the axial scan $I_{ax\rightarrow cor}$, as shown in Fig. 3a and 3c. In particular, $I_{ax\rightarrow cor}$ contains weaving patterns (Fig. 7.3c) while $LR_{zf,cor}$ is smooth overall (Fig. 7.3a; see the red arrows). This is because:

a) $LR_{zf,cor}$ does not account for the imaging characteristics due to the convolution of PSF_{SI} on I_{ax},
b) the 3 mm slice thickness of $LR_{zf,cor}$ (FWHM of PSF_{AP}) in the AP-direction is five times thicker than the 0.6 mm slice thickness of $I_{ax\rightarrow cor}$ in the AP-direction, and
c) the 3 mm voxel spacing of $LR_{zf,cor}$ (FWHM of PSF_{SI}) in the SI-direction is different than the 3.6 mm voxel spacing of $I_{ax\rightarrow cor}$ in the SI-direction (DS_{SI}).

To address the above three differences, we transform both I_{cor} and I_{ax} to the common LR image domain by considering both PSF_{AP} and PSF_{SI}. To synthesize the training input with I_{cor}, we convolve I_{cor} with PSF_{SI} (Fig. 8.2a):

$$LR_{cor}(x,y,z)|_{x\in[1,N_{LR}],y\in[1,NS_{AP}],z\in[1,NS_{SI}]}$$
$$= \sum_{k=z\times DS_{SI}-\left\lfloor\frac{L}{2}-1\right\rfloor}^{k=z\times DS_{SI}+\left\lfloor\frac{L}{2}\right\rfloor} PSF_{SI}(k)I_{cor}(x,y,k), \quad (4)$$

where LR_{cor} and I_{cor} form a LR-HR training pair for our deep generative networks (Fig. 8.4). The SR training output (SR_{cor}) has the same dimension and voxel size as the HR reference (I_{cor}).

For inference, we convolve I_{ax} with PSF_{AP} to form the convolved input $I_{ax,conv}$ (Fig. 5), defined as:

$$I_{ax,conv}(x,y,z)|_{x\in[1,N_{LR}],y\in[1,N_{AP}],z\in[1,NS_{SI}]}$$
$$= \sum_{j=y\times DS_{AP}-\left\lfloor\frac{L}{2}-1\right\rfloor}^{j=y\times DS_{AP}+\left\lfloor\frac{L}{2}\right\rfloor} PSF_{AP}(j)I_{ax}(x,j,z). \quad (5)$$

Note that the dimension is NY in the AP-direction, and we keep the matrix size of I_{ax} by applying a sliding window for the convolved input $I_{ax,conv}$.

Comparing the training input LR_{cor} and the inference input $I_{ax,conv}$ (Fig. 8.3b and 8.3d), both contain similar weaving artifacts in the SI-direction by considering both PSF_{AP} and PSF_{SI}. This is because the three physical problems are addressed by:

a) both LR_{cor} and $I_{ax,conv}$ that have multiplied with PSF_{SI} and PSF_{AP},

b) both LR_{cor} and $I_{ax,conv}$ that have the same 3 mm slice thickness in the AP-direction of FWHM of PSF_{AP}, and

c) both LR_{cor} and $I_{ax,conv}$ that have the same 3.6 mm voxel spacing in the SI-direction of DS_{SI}.

Thus, we ensure the input to the networks in training/validation, and the input in

the inference flow are of the consistent intrinsic voxel size and spacing.

8.2 Deep Generative Networks

Our SPTSR framework is model-agnostic, and the specific network architecture for deep generative networks was not the focus of our study. We adopted deep generative networks architecture largely from SRGAN [73], as shown in Fig. 8.4, with the three key differences. First, we used three consecutive low-resolution images as input, with the middle slice being the targeted input. By adding the adjacent slices to the original input, the networks can learn the spatial relationship between image slices. Because of imperfect slice excitation, the voxel information was intertwined between adjacent slices, further helping the model to generate super-resolution images. Compared to feeding the whole image volume into the networks, 3-slice input significantly lowers the overall graphical memory usage. Secondly, batch normalizations and the last sigmoid activation function were removed from the discriminator network because our networks were trained using WGAN-GP [74]. Lastly, the upsampling blocks in the generator model were modified to 1D anisotropic upsampling.

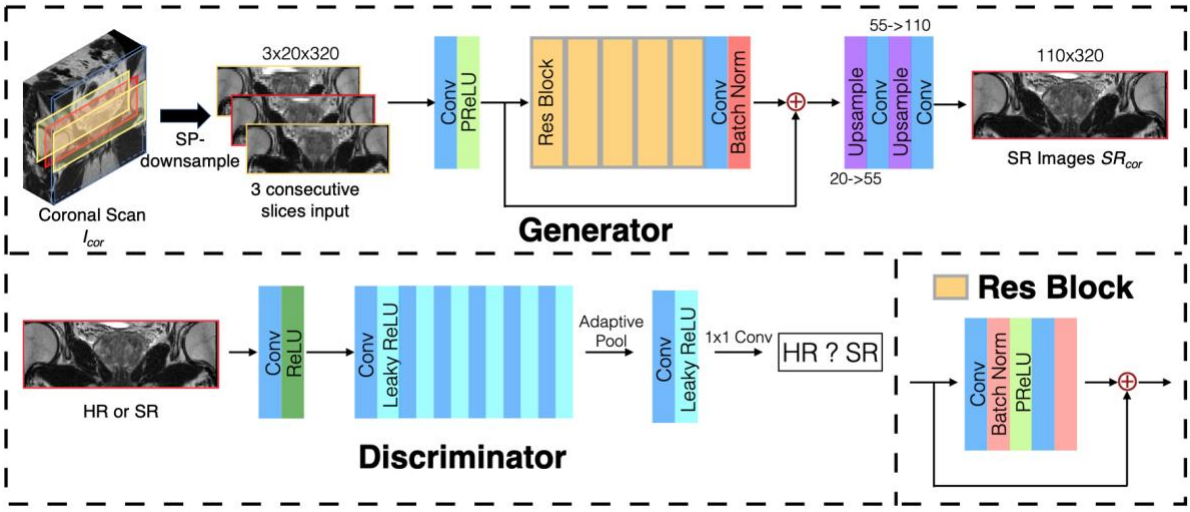

Figure 8.4: *The WGAN-GP based deep generative networks architecture of our proposed SPTSR framework.*

8.3 Inference Flow

The overall inference flow is shown in Fig. 8.5. Similar to the training 3-slice input, the input for inference contains three SP-convolved slices, including a center slice (red) and two adjacent slices (yellow). Note that the slices between training/validation input LR_{cor} have slice spacing of F_{AP}/NS_{AP}, so for the inference input $I_{ax,conv}$, the adjacent slices are also convolved at the physical distance of F_{AP}/NS_{AP} from the middle slice. Because the LR-HR training pairs are LR_{cor} and I_{cor}, the output from deep generative networks has the same voxel dimension and characteristics of I_{cor}. This applies to both the training/validation and inference pipeline. Each coronal plane slice of the inference output SR_{ax} is at the same resolution, matrix size and contrast compared to the cropped coronal scan I_{cor}. In addition, the inference output SR_{ax} is convolved in the AP-direction with an elongated voxel size, with the same matrix size F_{AP}/N_{AP} of I_{ax} in AP-direction. Thus, the inference through-plane SR output SR_{ax} not only synthesizes the coronal scan, but has an isotropic voxel spacing. To fully utilize this isotropic voxel spacing characteristic,

deconvolution, with the 1D slice profile PSF_{AP} (Fig. 8.5). The end product is the isotropic SR volume $SR_{ax,deconv}$. By using this iterative noise-robust Richardson-Lucy deconvolution method [75], [76], we transform the SR_{ax} with an elongated voxel size of $(\frac{F_{LR}}{N_{LR}}, \frac{F_{AP}}{NS_{AP}}, \frac{F_{SI}}{N_{SI}})$, to an isotropic high-resolution image volume$SR_{ax,deconv}$, with isotropic voxel size $(\frac{F_{LR}}{N_{LR}}, \frac{F_{AP}}{N_{AP}}, \frac{F_{SI}}{N_{SI}})$.

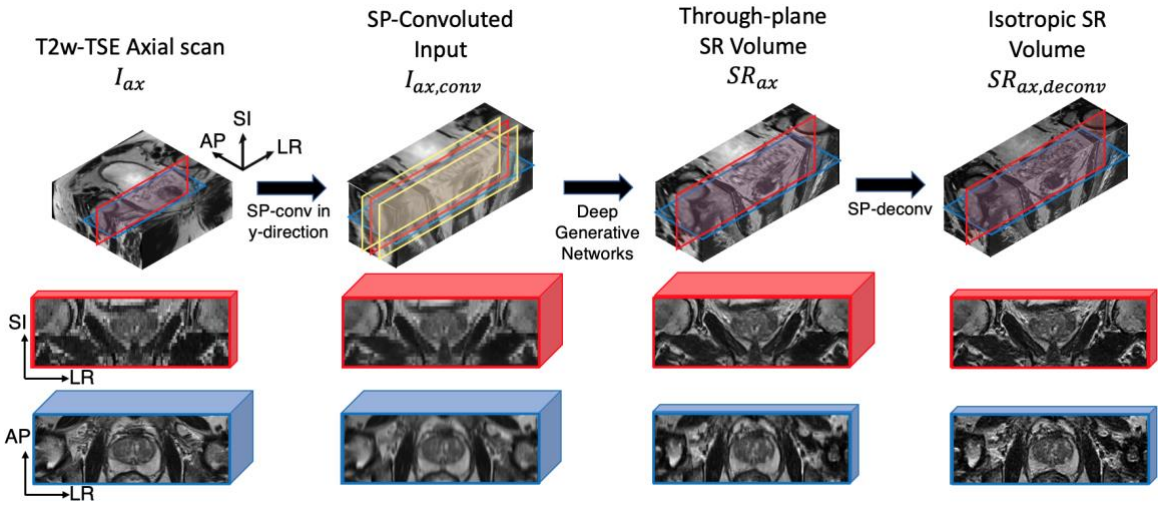

Figure 8.5: *The proposed SR inference flow. T2w-TSE axial scan is cropped and SP-convolved in the AP-direction to prepare the input for the deep generative networks. The output of the networks is still convolved in the AP-direction and is then transformed to isotropic SR volume via SP-deconvolution. Red patches represent coronal views and blue patches represent axial views. Patch thickness represents the voxel thickness in the through-plane of the patch.*

Chapter 9: 2D & 3D Experiments

9.1 Multi-slice 2D Experiments

9.1.1 MRI Dataset

We retrospectively reviewed clinical prostate MRI scans from March 2013 to December 2018 at a single academic institution and identified a total of 3,895 clinical subjects with 4,878 paired stacks of axial and coronal images using the multi-slice 2D T2-weighted turbo spin-echo (T2w-TSE) sequence. Institutional Review Board (IRB) approval was obtained for the study. The MRI scans were performed on one of several Siemens 3 Tesla scanners (including Prisma, Skyra, Vida, and Trio; Siemens Healthineers, Erlangen, Germany). Most clinical subjects had one pair of coronal and axial scans, and some subjects had more than one pair of scans at different time points. Both axial and coronal scans were based on the same imaging sequence except for the imaging-plane orientations. Each stack included 20 slices of T2w-TSE images, with an in-plane resolution of $0.625\times0.625\text{mm}^2$ (the matrix size of 320×320). The slice thickness was 3 mm with a slice spacing of 3.6 mm (i.e., a nominal gap of 0.6 mm between adjacent slice boundaries). No parallel imaging was used for reconstruction. The MRI sequence parameters are shown in Table 9.1.

Table 9.1: *The T2-weighted turbo spin-echo (T2w-TSE) sequence parameters*

TR/TE (ms)	4000/101
Refocusing angle (degree)	160
Bandwidth (Hz/pixel)	200
Acquisition matrix size	320×320
In-plane resolution (mm^2)	0.625×0.625
Number of slices	20
Slice thickness (mm)	3.0
Slice spacing (mm)	3.6
Number of averages	2
Scan time (mm:ss)	01:40×2

9.1.2 Data Preparation

The training/validation/testing splits were 3,453/392/50 from 3,895 clinical subjects. Training and validation used coronal scans. All of the training and validation coronal scans were cropped (320 to 110) in the z-direction to the same physical coverage distance as the axial scans. They were then downsampled by both the conventional KS-ZF and SP-downsampling methods to create separate training/validation datasets. Each coronal scan had 20 slices, generating 18 three-slice input samples.

The testing dataset used axial scans, and scans with strong inter-slice motion artifacts were manually excluded. The axial scans were reformatted to coronal orientation, which produced 320 slices of 20×320 reformatted images. They are also cropped (320 to 110) to have only imaging volumes of prostates overlapping with the coronal scans. The high-resolution coronal images were used as visual references.

9.1.3 Training Scheme

The deep generative networks were trained using the WGAN-GP scheme [74]. Thus, the discriminator loss included a weighted sum of the adversarial and gradient penalty loss. The generator loss included the weighted sum of the adversarial loss, mean-square-error (MSE) loss, and the VGG perceptual loss, where the weights were (10e-3, 1, 10e-6) respectively. The VGG perceptual loss showed excellent performance as a perceptual loss for super-resolution tasks [73], [77]. MSE of VGG-23 network output was used as the perceptual loss. The network was trained with 100 epochs, and the actual epoch was determined with the lowest validation MSE loss. The batch size was set to 64. Adam optimizer was used. The learning rate was 10e-4.

9.1.4 Through-plane SR Results

The output images after 5.5x through-plane SR are shown in Fig. 8.1. The T2w coronal and reformatted T2w axial scan images are shown as visual references, and the output results from bilinear interpolation, SMORE [62], KS-ZF trained networks, and SPTSR are compared to each other. The T2w coronal scan is used as a visual reference, not a ground truth, as it was acquired in a different scan. Both SMORE and KS-ZF trained networks removed most staircase and smearing artifacts compared to the simple bilinear interpolation but failed to reconstruct small structures within the prostate with amplified noise. The HR images produced by SPTSR are successfully containing small structures within the prostate, visually close to the T2w coronal scan images.

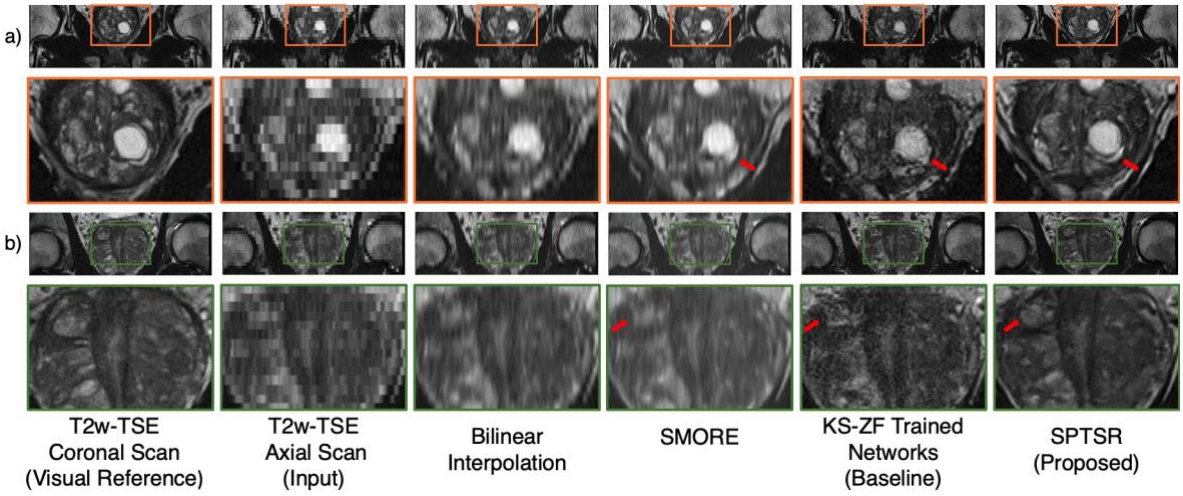

Figure 9.1: *The through-plane SR testing results with reformatted T2w axial scan input. a) and b) represents two image slices from two different testing subjects. From left to right: The T2w coronal scan of the subject, as a visual reference; the testing reformatted T2w axial scan as the inference input; the bilinear interpolation of the input; SMORE* [62]*; the baseline inference output with KS-ZF trained networks; the proposed SPTSR inference output with SP-downsampling trained network, and SP-convoluted inference input. Red arrows indicate the structural differences between the baseline results and the proposed results.*

9.1.5 Expert Reader Study

We designed our expert reader study, similar to the recent studies [39], [78], to assess the through-plane SR results with scans reformatted to coronal views. After a few training sessions, two genitourinary radiologists (M.Q. and C.S.; each had interpreted 500-1,500 prostate MRI scans with 5+ years of experience) independently assessed four methods: bilinear interpolation (BI), SMORE [62], KS-ZF trained networks (baseline), SPTSR (proposed). Any information indicating the type of processing was removed from all images and randomly shuffled for each subject when they were compared against the visual reference of HR in-plane T2w-TSE coronal scan of the same subject. All five image sets were simultaneously loaded into OsiriX (Pixmeo SARL, Bernex, Switzerland) and the reader scrolled through the coronal slices. Four methods all have a 5.5x number of slices as the original coronal scan, within the same physical distance. In total, 50 subjects (each with one axial scan) of the testing dataset were examined. Diagnostic quality metrics of sharpness (1: severe blurring, 2: moderate blurring, 3: mild blurring, and 4: no blurring), artifacts (1: severe artifacts, 2: moderate artifacts, 3: mild artifacts, and 4: no artifacts), noise level (1: severe noise, 2: moderate noise, 3: mild noise, and 4: no noise) and overall diagnostic image quality (1: severe, 2: moderate, 3: good, and 4: excellent) of each method were scored on a 4-point quality scale. The reader also blindly ranked the overall quality of the four methods against each other. The visual reference of the HR coronal scans was considered as the score 4 in all metrics. The coronal scans were not considered as ground-truth because they were separate scans from the axial scans and did not align precisely in space due to the patient and rectal motion between scans.

Averaged ratings and rankings from two readers were compared between three methods. Mann-Whitney U tests were used to assess the significant differences ($p<0.01$)

between the four methods. Cohen's Kappa was calculated for inter-reader variability [79].

The image quality assessment of the output results (1: severe, 2: moderate, 3: good, and 4: excellent) conducted by the expert readers is shown in Fig. 8.2. In a blinded fashion, the SPTSR method received an almost perfect overall image quality score (all cases received 4.0 except three cases, which received 3.5). The SPTSR method has significantly better overall image quality¬¬ scores ($p<0.01$) compared to all other methods (BI, SMORE, and KS-ZF). For ranking results, the SPTSR method ranked the best in 48 cases agreed by both radiologists and best and second-best in 2 cases by two radiologists. The proposed SPTSR method is significantly better compared to the baseline KS-ZF trained network in terms of sharpness, noise level, and overall image quality ($p<0.01$). Although SMORE had the best artifact score, its overall image quality was limited by its poor sharpness quality, thus having its overall score worse than the baseline, and significantly worse than the proposed method. The image quality assessment substantially agreed between the two readers with Cohen's Kappa of 0.72 (95% confidence interval: 0.66-0.78).

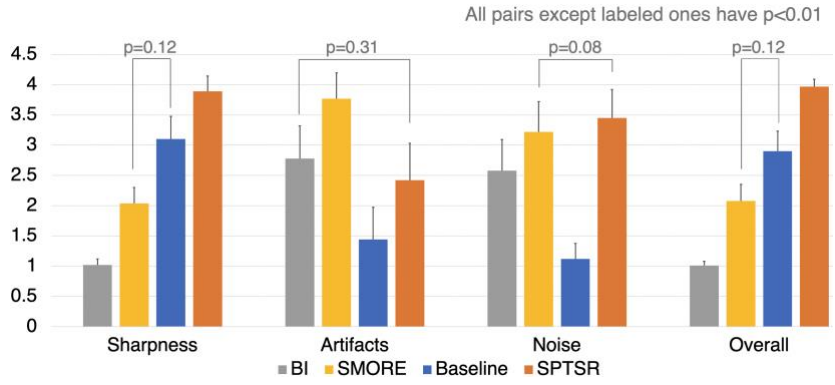

Figure 9.2: *Two radiologists qualitatively assessed the diagnostic quality of Bilinear Interpolation (BI), SMORE [8], KS-ZF trained networks (baseline), SPTSR (proposed), for sharpness, artifacts, noise and overall image quality on a 1 to 4 scale (higher the better). The ratings were averaged from two readers. Error bar represents the standard deviations. Mann-Whitney U tests assessed whether the average scores were significantly different ($p<0.01$) among the four groups.*

9.1.6 Quantitative Analysis

Quantitative analysis of the same four methods: BI, SMORE, baseline, and proposed method, was also performed to cross-validate with the qualitative reader study using the same 50-subject testing dataset. Because the visual reference coronal scans were not aligned pixel-by-pixel with the SR images, metrics such as peak signal-to-noise ratio (PSNR) or structural similarity index (SSIM) were not suitable here. Fréchet inception distance (FID) is one of the most common metrics for assessing the quality of images generated by generative models, for both natural images and MRI images [80]–[83]. Real and generated images were fed through a pre-trained inception network, and the FID measured the distance of the distributions between their activation output without requiring for pixel-wise alignment with the reference [80], [81].

For each method, 1,995 pairs of real and generated images are used to calculate FID. Each pair of images are cropped to 110×320 at the same scanner physical locations. The Mann-Whitney U test was used to assess the statistical differences between the four

methods.

The testing image quantitative assessment with FID is shown in Table 8.2. For each method, the FIDs of 1,995 images are shown as mean ± standard deviation (SD). Mann-Whitney U tests confirmed significant differences between each pair of methods ($p<0.01$). The FID results matched the overall image quality scores in the expert reader study. The proposed SPTSR method achieved the best FID scores. This quantitative analysis confirmed the proposed method has the best image visual quality.

***Table 9.2**: Testing quantitative results with FID*

Bilinear Interpolation	32.0 ± 12.5
SMORE [62]	29.5 ± 14.8
K-space Zero-fill	26.8 ± 10.4
SPTSR	**18.6± 8.5**

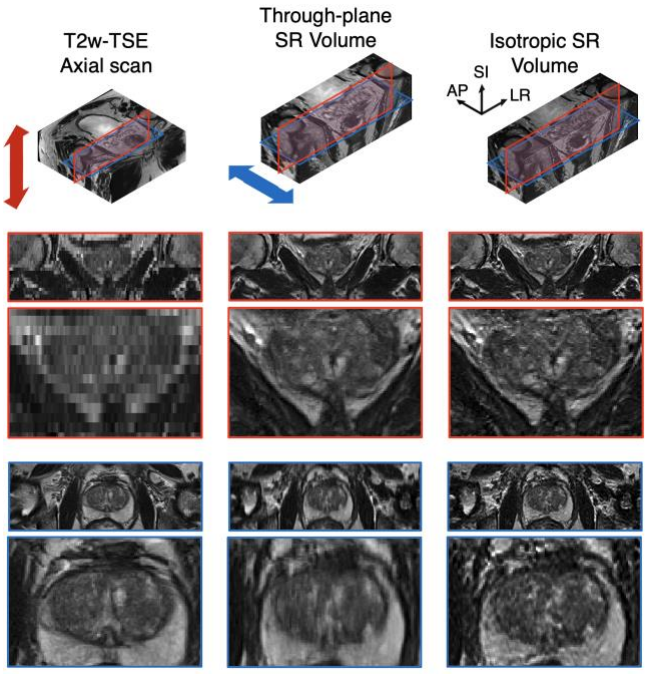

***Figure 9.3:** The isotropic SR output (right), compared to the original T2w-TSE axial scan input (left) and through-plane SR volume (middle) with elongated voxel. Two-sided arrows indicate the orientations of the slice-profile PSF as the blur kernel. Red patches represent coronal views and blue patches represent axial views.*

9.1.7 Isotropic SR Results

Fig. 9.2. shows the SP-deconvolved isotropic SR results from the through-plane SR image volume. The through-plane results have convolved by the same slice-profile PSF of the orthogonal axial scan, so even though it has an isotropic voxel spacing, its image in the original coronal plane is blurred by the slice-profile and does not retain its sharpness, compared to the coronal scan input. After the SP-deconv via Richardson-Lucy deconvolution in the AP-direction [75], [76], the blurring artifacts in the coronal plane are deblurred, resulting in an isotropic image volume with non-overlapping cubic voxels.

9.2 3D Simulation Experiments

3D simulation experiments were also conducted to further evaluate the effectiveness of SPTSR compared with 3D T2w as ground-truth.

9.2.1 MRI Datatset

We retrospectively reviewed clinical prostate MRI scans from March 2013 to December 2018 at a single academic institution and identified a total of 4,637 clinical subjects with 5,848 scans using the 3D T2w-TSE (SPACE) sequence. Institutional Review Board (IRB) approval was obtained for the study. The MRI scans were performed on one of several 3 Tesla scanners (including Prisma, Skyra, Vida, and Trio; Siemens Healthineers, Erlangen, Germany). The sequence parameters are shown in Table 8.3.

Table 9.3*: The 3D T2-weighted SPACE sequence parameters*

TR/TE (ms)	2200/201
Refocusing angle (degree)	100
Bandwidth (Hz/pixel)	315
Acquisition matrix size	256×256×60
In-plane resolution (mm^2)	0.664×0.664
Slice thickness (mm)	1.5
Scan time (mm:ss)	07:00

9.2.2 Data Preparation

The training/validation/testing splits were 4,080/464/93 from 4,637 clinical subjects. Each 3D scan volume was first interpolated to isotropic grid with voxel resolution of $1mm^3$, with a matrix size of (170×170×90).

The isotropic 3D volume was then center-cropped and SP-downsampled, with a 3mm truncated sinc PSF and 4mm slice thickness (4× downsampling). The training/validation datasets were SP-downsampled along the SI direction, simulating 2D T2w-TSE axial scans, whereas the testing datasets were SP-downsampled along the LR direction, simulating 2D T2w-TSE sagittal scans.

9.2.3 Training and Inference Schemes

Training schemes and inference flows for 3D simulation experiments followed the procedures of 2D T2w-TSE experiments. The simulated 2D T2w-TSE axial scans for training/validation were SP-downsampled along the LR direction to train/validate the deep generative networks. For testing, the simulated 2D T2w-TSE sagittal scans were inferenced through the trained deep generative networks and SP-deconvolved to reach 4× isotropic super-resolution of the original 1mm3 voxel size.

9.2.4 Isotropic SR Results

The simulated 2D sagittal scans input, SMORE and SPTSR results were compared against the isotropic 3D T2w ground-truth in all three orientations, as shown in Fig. 9. The images from SMORE were noticeably blurry in the super-resolved coronal and axial views, while the images from SPTSR considerably match well with the 3D T2w ground-truth in all three views.

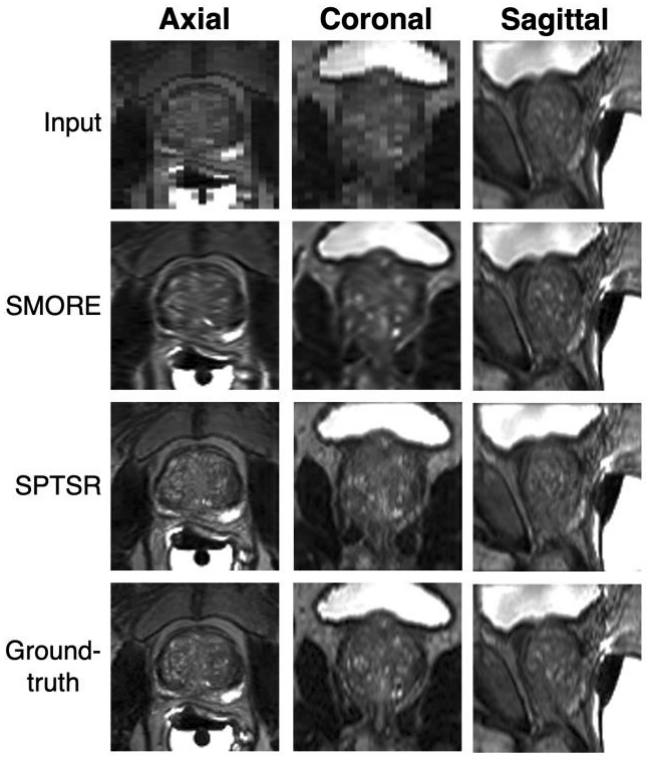

Figure 9.4: *Simulation experiments result with 3D T2w scans. Simulated 2D sagittal input, SMORE result, SPTSR result were compared with isotropic high-resolution ground-truth images in all three views.*

9.2.5 Quantitative Analysis

The simulation experiments have 3D isotropic high-resolution ground-truth volumes. Peak signal-to-noise ratio (PSNR) and normalized MSE (NMSE) were measured for each super-resolution output volume compared to the 3D T2w ground-truth.

For each method of SMORE, before-deconv, and after-deconv (SPTSR), 118 3D volumes from 93 testing subjects were used to calculate volumetric PSNR and NMSE. Mean and standard deviations were calculated, and paired samples t-test were conducted between each pair of method to evaluate statistical significance [84].

The PSNR and NMSE measurements for simulation experiment are shown in

Table 9.3. For each method, the PSNR and NMSE of 118 3D volumes are shown as mean ± SD. Paired samples t-test confirmed significant differences ($p<0.01$) between each pair of methods for both PSNR and NMSE.

The numerical results indicated that the proposed SPTSR method can super-resolve to isotropic high-resolution volume, and performs significantly better than SMORE when super-resolving images to isotropic high-resolution volume. This result also indicated that the final SP-deconvolution step is necessary to achieve high-quality isotropic super-resolution.

Table 9.4: *Simulation testing quantitative results with PSNR and NMSE*

	PSNR	NMSE ($\times 10^{-2}$)
SMORE [62]	26.81 ± 3.03	2.00 ± 1.15
Before SP-deconv	28.82 ± 2.90	1.00 ± 0.68
SPTSR	**29.08 ± 2.92**	**0.92 ± 0.54**

9.3 Ablation Studies

9.3.1 Individual Contributions from Two Improvements

To compare the separate contributions from the SP-downsampled input trained network and the SP-convolution pre-processed inference input, four methods were compared:

1) KS-ZF coronal scan training data, without SP-conv pre-processed axial scan inference testing data;
2) SP-DS coronal scan training data, without SP-conv pre-processed axial scan inference testing data;
3) KS-ZF coronal scan training data, with SP-conv pre-processed axial scan

inference testing data;

4) SP-DS coronal scan training data, with SP-conv pre-processed axial scan inference testing data (Proposed);

The comparison results are as shown in Fig. 9.3. Without either SP-downsampled training input or the SP-conv pre-processed inference input, the inference results did not achieve the desired sharpness and noise level, and could not fully recover the structural details.

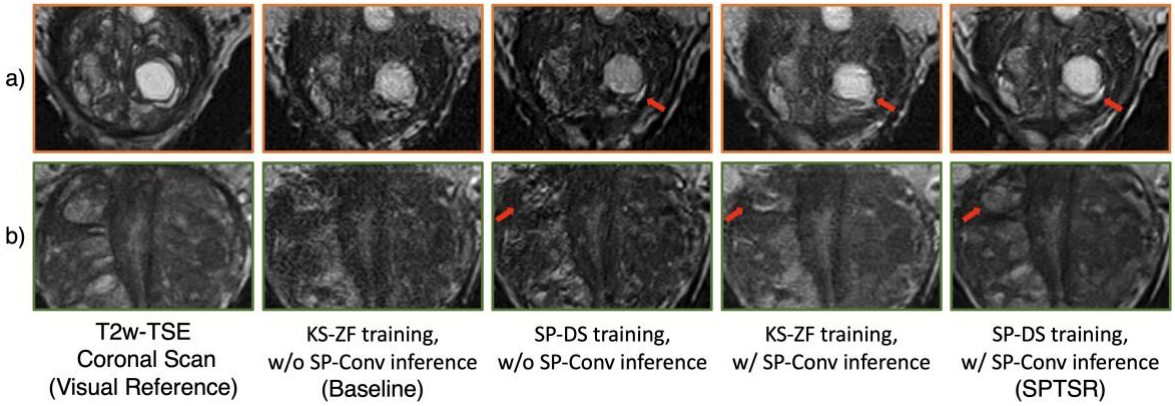

Figure 9.5: *Individual impact of SP-DS Network and SP-Conv input on testing output. a) and b) represents images from two different testing subjects, same as Fig. 8.1. From left to right: The T2w coronal scan of the subject, as a visual reference; the baseline KS-ZF downsampling method trained network, without SP-Convolved inference input; SP-DS method trained network, without SP-Convolved inference input; KS-ZF downsampling method trained network, with SP-Convolved inference input; the proposed SPTSR inference output with SP-DS method trained network, and SP-convoluted inference input. Red arrows indicate the structural differences between different results.*

9.3.2 Network Architectures

Our proposed deep generative networks are compared against three other popular deep-learning networks structures, such as U-Net [85], ResUNet [86], and SRGAN [73], to demonstrate the compatibility of the SPTSR framework with other deep learning networks architecture. For each of all four networks, it is trained with

SP-downsampled training data for up to 60 epochs. The epoch with the minimal MSE loss in the validation dataset has been chosen as the converged trained networks. Synthetic validation input from the validation datasets is used to assess the network structure in the ablation study. LR SP-downsampled images were generated directly from their high-resolution coronal scans. Both PSNR and structural similarity index measure (SSIM) were used to quantify the quality of the network's structure ablation because they exactly matched with the ground truth HR coronal scan. The number of parameters of the networks is also compared.

SRGAN is a single-image super-resolution (SISR) network, originally for 2D isotropic super-resolution. The upsampling blocks are replaced with anisotropic upsampling blocks used in our proposed networks to match the input-to-output image size. Similarly, the anisotropic upsampling blocks are concatenated to the front of the networks for both U-Net and ResUNet because they are designed for the same input and output size. The input images for both U-Net and ResUNet have been replaced with 3-slice input, and both networks also use the same training scheme as the proposed networks for a fair comparison.

The networks architectures ablation study is presented in Table 9.4. We compared three popular network architectures to our proposed networks. In terms of quantitative image metrics in the validation dataset, our proposed architecture achieved the best mean PSNR of 24.64, and the best mean SSIM of 0.817. The PSNR and SSIM were close compared to the U-Net and ResUNet architecture, but those two networks are significantly larger in the number of parameters. Our comparison with U-Net and ResUNet demonstrates that our proposed SPTSR does not need a large

network to achieve excellent SR results. On the other hand, SRGAN has approximately the same number of parameters as our proposed network, but SRGAN has the worst PSNR and SSIM numbers among all the networks. Compared to SRGAN, the main improvement from our proposed network is the use of 3-slice input instead of SISR in the SRGAN structure. Because of the SP-convolved input, the image voxels overlap in the slice direction. The use of 3-slice input borrows image information from the adjacent slice, which not only helps the through-plane SR results but also preserves the inter-slice consistency across the image volume and benefits the isotropic SR results.

Table 9.5: *The Network Structure Ablation Study Validation Results Comparison*

	Number of Parameters	SSIM	PSNR
U-Net [85]	17.3M	0.811±0.033	24.48±1.66
ResUNet[86]	13.0M	0.797±0.041	24.41±1.62
SRGAN [73]	**0.5M**	0.808±0.032	24.30±1.73
SPTSR	**0.5M**	**0.817±0.031**	**24.64±1.67**

9.3.3 Size of the Training Dataset

The validation MSE loss versus the number of training steps for different sizes of the training dataset is plotted in Figure 8.4. When N=10, the training dataset was too small, and the networks training was quickly overfitted, as the validation MSE loss start to skyrocket after 5k training steps. The validation MSE loss plots were similar for N=100, 1000, and 3483. This indicates the size of training dataset is sufficient on the order of 100 subjects. This is mainly because our proposed networks used a relatively small number of parameters, as shown in Table 9.5.

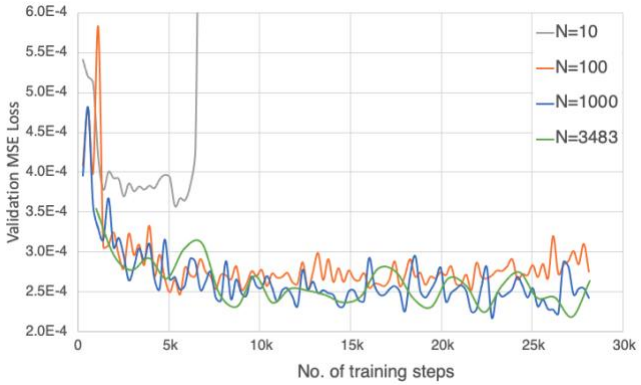

Figure 9.6: *The validation MSE loss with different sizes of the training dataset. The number of training dataset cases are 10, 100, 1000, and 3483 respectively. The MSE loss on the validation dataset is plotted against the number of training steps, with the same batch size.*

9.3.4 Slice Profiles

The slice profiles ablation study is presented in Table 8.5. Training and validating with datasets downsampled by truncated sinc produced better SSIM and PSNR results than other combinations, but all four comparisons showed no significant differences. Training and validating with Gaussian PSF had similar SSIM and PSNR compared to training and validating with truncated sinc PSF, indicating a slight inaccurate slice profile used does not affect the image quality; Training and validating with different slice profiles also had similar SSIM and PSNR, indicating retraining may not be required when the dataset included with different slice profiles was used.

Table 9.6: *The Slice Profiles Ablation Study With Gaussian PSF and Truncated Sinc PSF*

	SSIM	PSNR
Trained w/ Gaussian, validated w/ Gaussian	0.804±0.033	24.18±1.68
Trained w/ Gaussian, validated w/ trunc sinc	0.806±0.033	24.29±1.64
Trained w/ trunc sinc, validated w/ Gaussian	0.804±0.033	23.94±1.71
Trained w/ trunc sinc, validated w/ trunc sinc	**0.817±0.031**	**24.64±1.67**

Chapter 10: Discussions & Conclusions

We proposed a novel slice-profile transformation-based super-resolution (SPTSR) framework for multi-slice 2D TSE MRI. We utilized a large 2D/3D dataset of clinical subjects and scans and demonstrated the visual improvements for 5.5x through-plane SSR compared to the k-space zero-filling-based baseline method and the SMORE method. We also conducted 3D simulation experiments to demonstrate visual and quantitative improvements for 4x isotropic SSR compared to the 3D T2w ground-truth.

The testing output images for 2D clinical scans experiment were compared to the SMORE method [62], and a baseline KS-ZF trained network method. The output image quality was qualitatively evaluated on a 4-point Likert scale by two genitourinary radiologists in a blinded study. Quantitative analysis with FID was conducted to cross-validate with the reader study.

The testing output images for the 3D simulation experiment demonstrated the visual improvement of the SPTSR method compared to the SMORE method. The quantitative results of PSNR and NMSE confirmed the superiority of SPTSR. The quantitative comparison between before and after the last SP-deconvolution step indicated the effectiveness of the SP-deconvolution when achieving isotropic super-resolution.

The network structure ablation study justified our network structures and confirmed our SPTSR framework to be model-agnostic. The training dataset size ablation study confirmed that 2,000 images from 100 subjects were sufficient for network training because the proposed networks used a relatively small number of

parameters. The slice-profile ablation study confirmed that simulated slice profiles are sufficient for the SPTSR framework. Furthermore, we demonstrated the preliminary results of deconvolved isotropic SR from the through-plane SR image volumes.

In previous studies of super-resolution reconstruction (SSR), most approaches use multiple 2D scans, whereas our method only uses a single 2D scan for super-resolution. In previous studies for deep-learning-based super-resolution, most approaches consider the synthesis of LR images a single-image problem, opting for the k-space zero-fill or interpolation/averaging method [50]–[55], [57]–[60]. Our SPTSR method takes the slice profiles of both training and testing scans into consideration, jointly bridging the physical differences between training and testing data.

Compared to the baseline methods of using a KS-ZF trained network for the inference of orthogonal volumes, our proposed SPTSR methods output much sharper, less artifact, and much less noisy SR images. This is because there exist fundamental differences between training and testing data, as the conventional approaches did not take slice profiles into consideration. Our proposed method bridges the gap between the two by taking both slice profiles into consideration. The image results are strongly supported by our reader study results. The proposed SPTSR method received excellent overall image quality for 47 out of 50 cases, significantly better overall image quality than other methods ($p<0.01$). The quantitative analysis of FID with the testing dataset also confirmed the superiority in perceptual image quality of the proposed SPTSR method. This shows the effectiveness of SPTSR and the feasibility of

replacing multiple multi-slice 2D MRI scans with a single multi-slice 2D scan.

The proposed method combined SP-DS trained network and SP-convolution pre-processing to improve the overall image quality. Only changing the network from the baseline KS-ZF trained network to SP-DS trained network resulted in a sharper but noisier image compared to the proposed method. This is because the training input voxel is blurred by the slice-profile kernel in two orthogonal directions, whereas the inference input without SP-conv is blurred in only one direction. Only pre-processing the inference input with SP-convolution resulted in a smoother image, lacking sharpness and contrast. This is because the KS-ZF downsampled image is physically different from the inference input image.

In conclusion, we developed a novel slice-profile-transformation-based super-resolution (SPTSR) framework for the super-resolution of multi-slice 2D MRI scans. The proposed slice-profile transformations bridge the inherent physical mismatches between training and testing inputs due to an imperfect slice-selection profile. A large set of 4,878 pairs of axial and coronal MRI scans were used for training, validation, and testing of the proposed SPTSR framework. The expert reader study and experimental validation demonstrated the effectiveness of SPTSR in 5.5x through-plane SR with isotropic voxel spacing. Furthermore, we illustrated that SPTSR could achieve the isotropic SR with non-overlapping cubic voxels with the 3D simulation experiment.

Chapter 11: Future Work

We developed a novel SPTSR framework for isotropic super-resolution of multi-slice TSE MRI images. Three major areas can be further studied:

Clinical Applications

Our SPTSR framework is not limited to prostate imaging and can be applicable to a wide range of MRI applications. Multi-slice 2D MRI sequences are used in many different applications, including knee, prostate, brain, placenta, and fetal brain [36], [39], [41], [43], [87]. Typical clinical protocols for these applications require multiple orthogonal scans and can benefit from the SPTSR framework.

The benefit in clinical diagnosis from the increased resolution requires further validation. To demonstrate the clinical effectiveness of the SPTSR framework, experiments for downstream tasks, such as tumor detection, classification and segmentation can be performed. These experiments can further illustrate the clinical feasibility of replacing the multiple orthogonal scans in current clinical protocols with a single scan using our frameworks.

Network Architecture

Because our framework focuses on improving the training input synthesis and inference input pre-processing, our framework would not be limited to specific deep-learning architectures or training schemes. Thus, novel deep-learning method advancements can be applied jointly in future studies. Promising deep learning architectures include diffusion-based models and transformer-based models [88], [89].

In this work, a type of generative adversarial network (GAN) models was used for super-resolution. These generative models are prone to hallucination artifacts, which is detrimental to clinical assessment in medical images, especially if the model is optimized for high SSIM scores [90]. Specifically, in Fig 9.2, SPTSR frameworks have worse artifact levels than bilinear interpolation methods. This is largely due to the hallucination problems caused by GAN models. Recently, implicit neural representations (INR) have shown promising results for various tasks in computer visions, such as image synthesis [91], [92]. This is a possible direction for hallucination mitigation and has shown impressive results for MRI super-resolution [93].

Network Training Loss Design

Our framework included several limitations. First, current network training only considers the loss functions in through-plane SR. Deep-learning-based deconvolution methods [94], [95] enable self-consistency losses in the in-plane orientation, which can help further improve isotropic SR output. Second, our current approach does not account for inter-slice motion artifacts. In some applications, such as fetal brain MRI, motion is obvious and unavoidable [36], while patient motion during a typical prostate MRI scan is less significant [96], [97]. A more motion-robust SR framework can be achieved by including simulated motion in the training data, or enforcing a regularization loss term in the through-plane direction.

References

[1] J. Jagannathan *et al.*, "Outcome of using the histological pseudocapsule as a surgical capsule in Cushing disease," *J Neurosurg*, vol. 111, no. 3, pp. 531–539, 2009, doi: 10.3171/2008.8.JNS08339.

[2] O. Hamid, L. El Fiky, O. Hassan, A. Kotb, and S. El Fiky, "Anatomic Variations of the Sphenoid Sinus and Their Impact on Trans-sphenoid Pituitary Surgery," *Skull Base*, vol. 18, no. 1, p. 9, Jan. 2008, doi: 10.1055/S-2007-992764.

[3] A. A. de Rotte *et al.*, "Feasibility of high-resolution pituitary MRI at 7.0 tesla," *Eur Radiol*, vol. 24, no. 8, pp. 2005–2011, May 2014, doi: 10.1007/s00330-014-3230-x.

[4] M. C. Rossi Espagnet *et al.*, "High-resolution DCE-MRI of the pituitary gland using radial k-space acquisition with compressed sensing reconstruction," *AJNR Am J Neuroradiol*, vol. 36, no. 8, pp. 1444–1449, Aug. 2015, doi: 10.3174/ajnr.A4324.

[5] S. L. Tsai, E. Laffan, and S. Lawrence, "A retrospective review of pituitary MRI findings in children on growth hormone therapy.," *Pediatr Radiol*, vol. 42, no. 7, pp. 799–804, Jul. 2012, doi: 10.1007/s00247-012-2349-7.

[6] J. Cristante *et al.*, "Why We Should Still Treat by Neurosurgery Patients with Cushing Disease and a Normal or Inconclusive Pituitary MRI," *Journal of Clinical Endocrinology and Metabolism*, vol. 104, no. 12, pp. 5791–5792, 2019, doi: 10.1210/jc.2019-00333.

[7] Y. Grober, H. Grober, M. Wintermark, J. A. Jane, and E. H. Oldfield, "Comparison of MRI techniques for detecting microadenomas in Cushing's disease," *J Neurosurg*, vol. 128, no. 4, pp. 1051–1057, Apr. 2018, doi: 10.3171/2017.3.JNS163122.

[8] M. Varrassi *et al.*, "High-resolution magnetic resonance imaging at 3T of pituitary gland: Advantages and pitfalls," *Gland Surgery*, vol. 8(Suppl 3). pp. S208–S215, 2019. doi: 10.21037/gs.2019.06.08.

[9] A. Yao *et al.*, "Pituitary adenoma consistency: Direct correlation of ultrahigh field 7T MRI with histopathological analysis," *Eur J Radiol*, vol. 126, p. 108931, May 2020, doi: 10.1016/J.EJRAD.2020.108931.

[10] M. Law *et al.*, "Value of pituitary gland MRI at 7 T in Cushing's disease and relationship to inferior petrosal sinus sampling: Case report," *J Neurosurg*, vol. 1–5, Feb. 2018, doi: 10.3171/2017.9.JNS171969.

[11] B. Gruber, M. Froeling, T. Leiner, and D. W. J. Klomp, "RF coils: A practical guide for nonphysicists," *Journal of Magnetic Resonance Imaging*, vol. 48, no. 3, pp. 590–604, 2018, doi: 10.1002/jmri.26187.

[12] Y. Mazaheri, H. A. Vargas, G. Nyman, A. Shukla-Dave, O. Akin, and H. Hricak,

"Diffusion-weighted MRI of the prostate at 3.0 T: Comparison of endorectal coil (ERC) MRI and phased-array coil (PAC) MRI-THE impact of SNR on ADC measurement," *Eur J Radiol*, vol. 82, no. 10, pp. e515–e520, 2013, doi: 10.1016/j.ejrad.2013.04.041.

[13] P. Chittiboina *et al.*, "Endosphenoidal coil for intraoperative magnetic resonance imaging of the pituitary gland during transsphenoidal surgery," *J Neurosurg*, vol. 125, no. 6, pp. 1451–1459, 2016, doi: 10.3171/2015.11.JNS151465.

[14] M. Alfonsetti *et al.*, "Versatile coil design and positioning of transverse-field RF surface coils for clinical 1.5-T MRI applications," *MAGMA*, vol. 18, no. 2, pp. 69–75, 2005, doi: 10.1007/s10334-004-0090-4.

[15] O. Beuf, F. Pilleul, M. Armenean, G. Hadour, and H. Saint-Jalmes, "In vivo colon wall imaging using endoluminal coils: Feasibility study on rabbits," *Journal of Magnetic Resonance Imaging*, vol. 20, no. 1, pp. 90–96, Jul. 2004, doi: 10.1002/jmri.20059.

[16] A. Magill and R. Gruetter, "Nested Surface Coils for Multinuclear NMR," in *RF Coils for MRI*, J. T. Vaughan and J. R. Griffiths, Eds., 1 st.Chichester, UK: John Wiley & Sons, 2012, pp. 39–50. doi: 10.1002/9780470034590.emrstm1192.

[17] J. R. Hadley, L. Slusser, P. R. Merrill, E. Minalga, and L. D. Parker, "Remote Tuning and Matching of a Non-Resonant Wire Loop," in *ISMRM*, 2018.

[18] H. Kato *et al.*, "Development of a phantom compatible for MRI and hyperthermia using carrageenan gel--relationship between dielectric properties and NaCl concentration," *Int J Hyperthermia*, vol. 20, no. 5, pp. 529–538, Aug. 2004, doi: 10.1080/0265673042000199277.

[19] K. Yoshimura *et al.*, "Development of a tissue-equivalent MRI phantom using carrageenan gel," *Magn Reson Med*, vol. 50, no. 5, pp. 1011–1017, Nov. 2003, doi: 10.1002/mrm.10619.

[20] D. R. Messroghli, A. Radjenovic, S. Kozerke, D. M. Higgins, M. U. Sivananthan, and J. P. Ridgway, "Modified look-locker inversion recovery (MOLLI) for high-resolution T1 mapping of the heart," *Magn Reson Med*, vol. 52, no. 1, pp. 141–146, 2004, doi: 10.1002/mrm.20110.

[21] A. P. Amar and M. H. Weiss, "Pituitary anatomy and physiology," *Neurosurgery Clinics of North America*, vol. 14, no. 1. pp. 11–v, 2003. doi: 10.1016/S1042-3680(02)00017-7.

[22] C. D. Constantinides, E. Atalar, and E. R. McVeigh, "Signal-to-noise measurements in magnitude images from NMR phased arrays," *Magn Reson Med*, vol. 38, no. 5, pp. 852–857, 1997, doi: 10.1002/mrm.1910380524.

[23] P. Kellman and E. R. McVeigh, “Image reconstruction in SNR units: a general method for SNR measurement,” *Magn Reson Med*, vol. 54, no. 6, pp. 1439–1447, 2005, doi: 10.1002/mrm.20713.

[24] S. Solis-Najera, G. Cuellar, R. Wang, D. Tomasi, and A. Rodríguez, “Transceiver 4-leg birdcage for high field MRI: Knee imaging,” *Revista Mexicana de Física, ISSN 0035-001X, Vol. 54, Nº. 3, 2008, pags. 215-221*, vol. 54, 2009.

[25] G. Giovannetti *et al.*, “Conductor geometry and capacitor quality for performance optimization of low-frequency birdcage coils,” *Concepts Magn Reson Part B Magn Reson Eng*, vol. 20B, no. 1, pp. 9–16, 2004, doi: https://doi.org/10.1002/cmr.b.20005.

[26] D. Zhang and Y. Rahmat-Samii, “A Novel Flexible Electrotextile 3T MRI RF Coil Array for Carotid Artery Imaging: Design, Characterization, and Prototyping,” *IEEE Trans Antennas Propag*, vol. 67, no. 8, pp. 5115–5125, 2019, doi: 10.1109/TAP.2019.2891700.

[27] A. Macovski, “Noise in MRI,” *Magn Reson Med*, vol. 36, no. 3, pp. 494–497, Sep. 1996, doi: 10.1002/mrm.1910360327.

[28] C. M. Collins *et al.*, “Temperature and SAR calculations for a human head within volume and surface coils at 64 and 300 MHz,” *Journal of Magnetic Resonance Imaging*, vol. 19, no. 5, pp. 650–656, May 2004, doi: 10.1002/JMRI.20041.

[29] S. Aissani, E. Laistler, and J. Felblinger, “MR safety assessment of active implantable medical devices,” *Radiologe*, vol. 59, no. 1, pp. 40–45, Dec. 2019, doi: 10.1007/S00117-019-0541-6/METRICS.

[30] M. Zaitsev, J. Maclaren, and M. Herbst, “Motion artifacts in MRI: A complex problem with many partial solutions,” *Journal of Magnetic Resonance Imaging*, vol. 42, no. 4, pp. 887–901, Oct. 2015, doi: 10.1002/JMRI.24850.

[31] S. D. Serai *et al.*, “Newly developed methods for reducing motion artifacts in pediatric abdominal MRI: Tips and Pearls,” *American Journal of Roentgenology*, vol. 214, no. 5, pp. 1042–1053, May 2020, doi: 10.2214/AJR.19.21987.

[32] J. Y. Cheng *et al.*, “Free-breathing pediatric MRI with nonrigid motion correction and acceleration,” *Journal of Magnetic Resonance Imaging*, vol. 42, no. 2, pp. 407–420, Aug. 2015, doi: 10.1002/JMRI.24785.

[33] W. Jiang *et al.*, “Motion robust high resolution 3D free-breathing pulmonary MRI using dynamic 3D image self-navigator,” *Magn Reson Med*, vol. 79, no. 6, pp. 2954–2967, Jun. 2018, doi: 10.1002/MRM.26958.

[34] I. F. Harrison *et al.*, “Non-Invasive imaging of CSF-mediated brain clearance pathways via assessment of perivascular fluid movement with diffusion tensor

MRI," *Elife*, vol. 7, Jul. 2018, doi: 10.7554/ELIFE.34028.

[35] K. Haris *et al.*, "Self-gated fetal cardiac MRI with tiny golden angle iGRASP: A feasibility study," *Journal of Magnetic Resonance Imaging*, vol. 46, no. 1, pp. 207–217, Jul. 2017, doi: 10.1002/jmri.25599.

[36] M. Ebner *et al.*, "An automated framework for localization, segmentation and super-resolution reconstruction of fetal brain MRI," *Neuroimage*, vol. 206, p. 116324, Feb. 2020, doi: 10.1016/J.NEUROIMAGE.2019.116324.

[37] J. P. Mugler, "Optimized three-dimensional fast-spin-echo MRI," *Journal of Magnetic Resonance Imaging*, vol. 39, no. 4, pp. 745–767, Apr. 2014, doi: 10.1002/JMRI.24542.

[38] Y. Chen, F. Shi, A. G. Christodoulou, Y. Xie, Z. Zhou, and D. Li, "Efficient and accurate MRI super-resolution using a generative adversarial network and 3D multi-level densely connected network," in *Lecture Notes in Computer Science (including subseries Lecture Notes in Artificial Intelligence and Lecture Notes in Bioinformatics)*, Springer Verlag, 2018, pp. 91–99. doi: 10.1007/978-3-030-00928-1_11.

[39] A. S. Chaudhari *et al.*, "Super-resolution musculoskeletal MRI using deep learning," *Magn Reson Med*, vol. 80, no. 5, pp. 2139–2154, Nov. 2018, doi: 10.1002/mrm.27178.

[40] H. Greenspan, "Super-resolution in medical imaging," *Computer Journal*, vol. 52, no. 1, pp. 43–63, Jan. 2009, doi: 10.1093/COMJNL/BXM075.

[41] R. Sood and M. Rusu, "Anisotropic super resolution in prostate mri using super resolution generative adversarial networks," *Proceedings - International Symposium on Biomedical Imaging*, vol. 2019-April, no. Isbi, pp. 1688–1691, 2019, doi: 10.1109/ISBI.2019.8759237.

[42] R. Kijowski *et al.*, "Knee joint: Comprehensive assessment with 3D isotropic resolution fast spin-echo MR imaging - Diagnostic performance compared with that of conventional MR imaging at 3.0 T," *Radiology*, vol. 252, no. 2, pp. 486–495, Aug. 2009, doi: 10.1148/radiol.2523090028.

[43] J. Torrents-Barrena *et al.*, "Fully automatic 3D reconstruction of the placenta and its peripheral vasculature in intrauterine fetal MRI," *Med Image Anal*, vol. 54, pp. 263–279, May 2019, doi: 10.1016/J.MEDIA.2019.03.008.

[44] F. Rousseau *et al.*, "A novel approach to high resolution fetal brain MR imaging," *Med Image Comput Comput Assist Interv*, vol. 8, no. Pt 1, pp. 548–555, 2005, doi: 10.1007/11566465_68.

[45] S. Jiang, H. Xue, A. Glover, M. Rutherford, D. Rueckert, and J. V. Hajnal, "MRI of

moving subjects using multislice snapshot images with volume reconstruction (SVR): application to fetal, neonatal, and adult brain studies," *IEEE Trans Med Imaging*, vol. 26, no. 7, pp. 967–980, Jul. 2007, doi: 10.1109/TMI.2007.895456.

[46] A. Gholipour, J. A. Estroff, and S. K. Warfield, "Robust super-resolution volume reconstruction from slice acquisitions: Application to fetal brain MRI," *IEEE Trans Med Imaging*, vol. 29, no. 10, pp. 1739–1758, Oct. 2010, doi: 10.1109/TMI.2010.2051680.

[47] A. Gholipour *et al.*, "Super-resolution reconstruction in frequency, image, and wavelet domains to reduce through-plane partial voluming in MRI," *Med Phys*, vol. 42, no. 12, pp. 6919–6932, Dec. 2015, doi: 10.1118/1.4935149.

[48] T. Küstner *et al.*, "Deep-learning based super-resolution for 3D isotropic coronary MR angiography in less than a minute," *Magn Reson Med*, vol. 86, no. 5, pp. 2837–2852, Nov. 2021, doi: 10.1002/MRM.28911.

[49] J. Y. Lin, Y. C. Chang, and W. H. Hsu, "Efficient and Phase-Aware Video Super-Resolution for Cardiac MRI," in *Lecture Notes in Computer Science (including subseries Lecture Notes in Artificial Intelligence and Lecture Notes in Bioinformatics)*, Springer Science and Business Media Deutschland GmbH, 2020, pp. 66–76. doi: 10.1007/978-3-030-59719-1_7.

[50] C.-H. Pham, A. Ducournau, R. Fablet, and F. Rousseau, "Brain MRI super-resolution using deep 3D convolutional networks," in *2017 IEEE 14th International Symposium on Biomedical Imaging (ISBI 2017)*, IEEE, Apr. 2017, pp. 197–200. doi: 10.1109/ISBI.2017.7950500.

[51] Y. Zheng, B. Zhen, A. Chen, F. Qi, X. Hao, and B. Qiu, "A hybrid convolutional neural network for super-resolution reconstruction of MR images," *Med Phys*, vol. 47, no. 7, pp. 3013–3022, Jul. 2020, doi: 10.1002/mp.14152.

[52] J. Shi *et al.*, "MR Image Super-Resolution via Wide Residual Networks with Fixed Skip Connection," *IEEE J Biomed Health Inform*, vol. 23, no. 3, pp. 1129–1140, May 2019, doi: 10.1109/JBHI.2018.2843819.

[53] K. Zeng, H. Zheng, C. Cai, Y. Yang, K. Zhang, and Z. Chen, "Simultaneous single- and multi-contrast super-resolution for brain MRI images based on a convolutional neural network," *Comput Biol Med*, vol. 99, pp. 133–141, Aug. 2018, doi: 10.1016/J.COMPBIOMED.2018.06.010.

[54] H. Zheng *et al.*, "Multi-Contrast Brain MRI Image Super-Resolution with Gradient-Guided Edge Enhancement," *IEEE Access*, vol. 6, pp. 57856–57867, 2018, doi: 10.1109/ACCESS.2018.2873484.

[55] Y. Chen, Y. Xie, Z. Zhou, F. Shi, A. G. Christodoulou, and D. Li, "Brain MRI super resolution using 3D deep densely connected neural networks," *Proceedings* -

International Symposium on Biomedical Imaging, vol. 2018-April, pp. 739–742, May 2018, doi: 10.1109/ISBI.2018.8363679.

[56] Y. Chen, A. G. Christodoulou, Z. Zhou, F. Shi, Y. Xie, and D. Li, "MRI Super-Resolution with GAN and 3D Multi-Level DenseNet: Smaller, Faster, and Better," *arXiv:2003.01217*, Mar. 2020, doi: 10.48550/arxiv.2003.01217.

[57] Q. Lyu *et al.*, "Multi-Contrast Super-Resolution MRI through a Progressive Network," *IEEE Trans Med Imaging*, vol. 39, no. 9, pp. 2738–2749, Sep. 2020, doi: 10.1109/TMI.2020.2974858.

[58] E. M. Masutani, N. Bahrami, and A. Hsiao, "Deep Learning Single-Frame and Multiframe Super-Resolution for Cardiac MRI," *Radiology*, vol. 295, no. 3, pp. 552–561, Apr. 2020, doi: 10.1148/RADIOL.2020192173.

[59] J. Wang, Y. Chen, Y. Wu, J. Shi, and J. Gee, "Enhanced generative adversarial network for 3D brain MRI super-resolution," *Proceedings - 2020 IEEE Winter Conference on Applications of Computer Vision, WACV 2020*, pp. 3616–3625, Mar. 2020, doi: 10.1109/WACV45572.2020.9093603.

[60] Q. Lyu, C. You, H. Shan, Y. Zhang, and G. Wang, "Super-resolution MRI and CT through GAN-CIRCLE," *Developments in X-ray tomography XII*, vol. 11113, pp. 202–208, Sep. 2019, doi: 10.1117/12.2530592.

[61] H. Liu, E. Michel, S. O. Casey, and C. L. Truwit, "Actual imaging slice profile of 2D MRI," *Medical Imaging 2002: Physics of Medical Imaging*, vol. 4682, no. 3, pp. 767–773, May 2002, doi: 10.1117/12.465627.

[62] C. Zhao, B. E. Dewey, D. L. Pham, P. A. Calabresi, D. S. Reich, and J. L. Prince, "SMORE: A Self-Supervised Anti-Aliasing and Super-Resolution Algorithm for MRI Using Deep Learning," *IEEE Trans Med Imaging*, vol. 40, no. 3, pp. 805–817, Mar. 2021, doi: 10.1109/TMI.2020.3037187.

[63] H. Greenspan, G. Oz, N. Kiryati, and S. Peled, "MRI inter-slice reconstruction using super-resolution," *Magn Reson Imaging*, vol. 20, no. 5, pp. 437–446, Jun. 2002, doi: 10.1016/S0730-725X(02)00511-8.

[64] F. Odille *et al.*, "Isotropic 3D cardiac cine MRI allows efficient sparse segmentation strategies based on 3D surface reconstruction," *Magn Reson Med*, vol. 79, no. 5, pp. 2665–2675, May 2018, doi: 10.1002/MRM.26923/ASSET/SUPINFO/MRM26923-SUP-0001-SUPPINFO01.DOCX.

[65] N. C. Askin Incebacak *et al.*, "Super-resolution reconstruction of T2-weighted thick-slice neonatal brain MRI scans," *Journal of Neuroimaging*, vol. 32, no. 1, pp. 68–79, Jan. 2022, doi: 10.1111/jon.12929.

[66] W. Yuan *et al.*, "Accurate Prenatal Diagnosis of Cleft Palate Using Magnetic

Resonance Imaging with Slice-to-Volume Reconstruction," *Applied Magnetic Resonance 2019 51:1*, vol. 51, no. 1, pp. 23–32, Oct. 2019, doi: 10.1007/S00723-019-01161-5.

[67] W. Yang, X. Zhang, Y. Tian, W. Wang, J. H. Xue, and Q. Liao, "Deep Learning for Single Image Super-Resolution: A Brief Review," *IEEE Trans Multimedia*, vol. 21, no. 12, pp. 3106–3121, Dec. 2019, doi: 10.1109/TMM.2019.2919431.

[68] T. A. Gallagher, A. J. Nemeth, and L. Hacein-Bey, "An Introduction to the Fourier Transform: Relationship to MRI," *AJR Am J Roentgenol*, vol. 190, no. 5, pp. 1396–1405, Nov. 2008, doi: 10.2214/AJR.07.2874.

[69] J. Jurek, M. Kociński, A. Materka, M. Elgalal, and A. Majos, "CNN-based superresolution reconstruction of 3D MR images using thick-slice scans," *Biocybern Biomed Eng*, vol. 40, no. 1, pp. 111–125, Jan. 2020, doi: 10.1016/J.BBE.2019.10.003.

[70] K. Zhang *et al.*, "SOUP-GAN: Super-Resolution MRI Using Generative Adversarial Networks," *Tomography*, vol. 8, no. 2, p. 905, Mar. 2022, doi: 10.3390/TOMOGRAPHY8020073.

[71] K. K. Bhatia, A. N. Price, W. Shi, J. V. Hajnal, and D. Rueckert, "Super-resolution reconstruction of cardiac MRI using coupled dictionary learning," *2014 IEEE 11th International Symposium on Biomedical Imaging, ISBI 2014*, pp. 947–950, Jul. 2014, doi: 10.1109/ISBI.2014.6868028.

[72] R. R. Sood *et al.*, "3D Registration of pre-surgical prostate MRI and histopathology images via super-resolution volume reconstruction," *Med Image Anal*, vol. 69, p. 101957, Apr. 2021, doi: 10.1016/J.MEDIA.2021.101957.

[73] C. Ledig *et al.*, "Photo-Realistic Single Image Super-Resolution Using a Generative Adversarial Network," *Cvpr*, vol. 2, no. 3, p. 4, 2017.

[74] I. Gulrajani, F. Ahmed, M. Arjovsky, V. Dumoulin, and A. Courville, "Improved training of wasserstein GANs," *Adv Neural Inf Process Syst*, vol. 2017-Decem, pp. 5768–5778, 2017.

[75] W. H. Richardson, "Bayesian-Based Iterative Method of Image Restoration*," *JOSA, Vol. 62, Issue 1, pp. 55-59*, vol. 62, no. 1, pp. 55–59, Jan. 1972, doi: 10.1364/JOSA.62.000055.

[76] L. B. Lucy, "An iterative technique for the rectification of observed distributions," *Astron J*, vol. 79, no. 6, p. 745, 1974, doi: 10.1086/111605.

[77] J. Johnson, A. Alahi, and L. Fei-Fei, "Perceptual losses for real-time style transfer and super-resolution," *ECCV 2016. Lecture Notes in Computer Science*, vol. 9906 LNCS, pp. 694–711, 2016, doi: 10.1007/978-3-319-46475-6_43.

[78] B. Yaman, S. A. H. Hosseini, S. Moeller, J. Ellermann, K. Uğurbil, and M. Akçakaya, "Self-supervised learning of physics-guided reconstruction neural networks without fully sampled reference data," *Magn Reson Med*, vol. 84, no. 6, pp. 3172–3191, Dec. 2020, doi: 10.1002/MRM.28378.

[79] M. L. McHugh, "Interrater reliability: the kappa statistic," *Biochem Med (Zagreb)*, vol. 22, no. 3, p. 276, 2012.

[80] M. Heusel, H. Ramsauer, T. Unterthiner, B. Nessler, and S. Hochreiter, "GANs trained by a two time-scale update rule converge to a local Nash equilibrium," in *Advances in Neural Information Processing Systems*, 2017, pp. 6627–6638.

[81] K. Shmelkov, C. Schmid, and K. Alahari, "How Good Is My GAN?," in *Proceedings of the European Conference on Computer Vision (ECCV)*, 2018, pp. 213–229. doi: 10.1007/978-3-030-01216-8_14.

[82] M. Jiang *et al.*, "FA-GAN: Fused attentive generative adversarial networks for MRI image super-resolution," *Computerized Medical Imaging and Graphics*, vol. 92, p. 101969, Sep. 2021, doi: 10.1016/j.compmedimag.2021.101969.

[83] J. Lv, J. Zhu, and G. Yang, "Which GAN? A comparative study of generative adversarial network-based fast MRI reconstruction," *Philosophical Transactions of the Royal Society A: Mathematical, Physical and Engineering Sciences*, vol. 379, no. 2200, Jun. 2021, doi: 10.1098/rsta.2020.0203.

[84] A. Ross and V. L. Willson, "Paired Samples T-Test," *Basic and Advanced Statistical Tests*, pp. 17–19, 2017, doi: 10.1007/978-94-6351-086-8_4.

[85] O. Ronneberger, P. Fischer, and T. Brox, "U-Net: Convolutional Networks for Biomedical Image Segmentation," *Lecture Notes in Computer Science (including subseries Lecture Notes in Artificial Intelligence and Lecture Notes in Bioinformatics)*, vol. 9351, pp. 234–241, 2015, doi: 10.1007/978-3-319-24574-4_28.

[86] Z. Zhang, Q. Liu, and Y. Wang, "Road Extraction by Deep Residual U-Net," *IEEE Geoscience and Remote Sensing Letters*, vol. 15, no. 5, pp. 749–753, May 2018, doi: 10.1109/LGRS.2018.2802944.

[87] S. Aslani, M. Dayan, V. Murino, and D. Sona, "Deep 2D Encoder-Decoder Convolutional Neural Network for Multiple Sclerosis Lesion Segmentation in Brain MRI," *Lecture Notes in Computer Science (including subseries Lecture Notes in Artificial Intelligence and Lecture Notes in Bioinformatics)*, vol. 11383 LNCS, pp. 132–141, Sep. 2018, doi: 10.1007/978-3-030-11723-8_13.

[88] J. Ho, A. Jain, and P. Abbeel, "Denoising Diffusion Probabilistic Models," *Adv Neural Inf Process Syst*, vol. 33, pp. 6840–6851, 2020, Accessed: Aug. 27, 2023. [Online]. Available: https://github.com/hojonathanho/diffusion.

[89] G. Li *et al.*, “Transformer-Empowered Multi-Scale Contextual Matching and Aggregation for Multi-Contrast MRI Super-Resolution,” *Proceedings of the IEEE/CVF Conference on Computer Vision and Pattern Recognition (CVPR)*. pp. 20636–20645, 2022.

[90] M. J. Muckley *et al.*, “Results of the 2020 fastMRI Challenge for Machine Learning MR Image Reconstruction,” *IEEE Trans Med Imaging*, vol. 40, no. 9, pp. 2306–2317, Sep. 2021, doi: 10.1109/TMI.2021.3075856.

[91] B. Mildenhall, P. P. Srinivasan, M. Tancik, J. T. Barron, R. Ramamoorthi, and R. Ng, “NeRF: Representing Scenes as Neural Radiance Fields for View Synthesis,” *Commun ACM*, vol. 65, no. 1, 2022, doi: 10.1145/3503250.

[92] V. Sitzmann, M. Zollhöfer, and G. Wetzstein, “Scene Representation Networks: Continuous 3D-Structure-Aware Neural Scene Representations”.

[93] J. Xu *et al.*, “NeSVoR: Implicit Neural Representation for Slice-to-Volume Reconstruction in MRI,” *IEEE Trans Med Imaging*, vol. 42, no. 6, pp. 1707–1719, Jun. 2023, doi: 10.1109/TMI.2023.3236216.

[94] L. Xu, J. S. Ren, C. Liu, and J. Jia, “Deep Convolutional Neural Network for Image Deconvolution,” *Adv Neural Inf Process Syst*, vol. 27, 2014.

[95] J. Dong, S. Roth, and B. Schiele, “Deep Wiener Deconvolution: Wiener Meets Deep Learning for Image Deblurring,” *Adv Neural Inf Process Syst*, vol. 2020-December, Mar. 2021.

[96] C. Malamateniou *et al.*, “Motion-Compensation Techniques in Neonatal and Fetal MR Imaging,” *American Journal of Neuroradiology*, vol. 34, no. 6, pp. 1124–1136, Jun. 2013, doi: 10.3174/AJNR.A3128.

[97] M. J. Ghilezan *et al.*, “Prostate gland motion assessed with cine-magnetic resonance imaging (cine-MRI),” *International Journal of Radiation Oncology*Biology*Physics*, vol. 62, no. 2, pp. 406–417, Jun. 2005, doi: 10.1016/J.IJROBP.2003.10.017.